

# Monte Carlo Simulations of Globular Cluster Evolution. V. Binary Stellar Evolution

Sourav Chatterjee<sup>1</sup>, John M. Fregeau<sup>2,3</sup>, Stefan Umbreit<sup>1</sup>, and Frederic A. Rasio<sup>1</sup>

<sup>1</sup> *Department of Physics and Astronomy, Northwestern University, Evanston, IL 60208, USA*

<sup>2</sup> *Kavli Institute for Theoretical Physics, UCSB, Santa Barbara, CA 93106, USA*

<sup>3</sup> *Chandra/Einstein Fellow*

## ABSTRACT

We study the dynamical evolution of globular clusters containing primordial binaries, including full single and binary stellar evolution using our Monte Carlo cluster evolution code updated with an adaptation of the single and binary stellar evolution codes SSE/BSE from Hurley et al. (2000, 2002). We describe the modifications we have made to the code. We present several test calculations and comparisons with existing studies to illustrate the validity of the code. We show that our code finds very good agreement with direct  $N$ -body simulations including primordial binaries and stellar evolution. We find significant differences in the evolution of the global properties of the simulated clusters using stellar evolution compared to simulations without any stellar evolution. In particular, we find that the mass loss from stellar evolution acts as a significant energy production channel simply by reducing the total gravitational binding energy and can significantly prolong the initial core contraction phase before reaching the binary-burning quasi steady state of the cluster evolution as noticed in Paper IV. We simulate a large grid of clusters varying the initial cluster mass, binary fraction, and concentration and compare properties of the simulated clusters with those of the observed Galactic globular clusters (G GCs). We find that our simulated cluster properties agree well with the observed G GC properties. We explore in some detail qualitatively different clusters in different phases of their evolution, and construct synthetic Hertzsprung-Russell diagrams for these clusters.

## 1. Introduction

Star clusters in general, and the Galactic globular clusters in particular, have been studied extensively for many years. As tracers of the Galaxy's potential, their dynamical

history tells us something about the formation and evolution of our Galaxy. As dense stellar environments, their interesting constituent populations (including, e.g., blue straggler stars, cataclysmic variables, and low-mass X-ray binaries) inform our understanding of binary stellar evolution through its interaction with dynamics. The study of the evolution of globular and other dense star clusters has had a somewhat long and varied history (e.g., Heggie & Hut 2003). Before observations showed that globular clusters contained dynamically significant numbers of binaries, theoretical efforts focused on understanding the process of core collapse and the ensuing post-collapse evolution driven by three-body binary formation. Once it became clear in the early 90s from observations that clusters contained sufficient numbers of binaries that they must have been born with substantial “primordial” populations, theory emphasized properties of clusters in the “binary burning” phase, in which the cluster core is supported against collapse by super-elastic dynamical scattering interactions of binary stars. More recently it has been realized that pure point-mass interactions of binaries result in equilibrium cluster core radii in the binary burning phase that are a factor of  $\sim 10$  smaller than what is observed, and so many efforts have focused on alternative cluster energy sources such as central intermediate-mass black holes, expedited stellar mass loss from compact object formation via collisions, or prolonged mass segregation of compact objects (Heggie et al. 2006; Fregeau & Rasio 2007; Trenti 2006; Chatterjee et al. 2008; Merritt et al. 2004). In a similar vein, recent theoretical work, combined with observations showing that the core binary fraction in many clusters is fairly low ( $\lesssim 10\%$ ), suggest that clusters may be born with remarkably low binary fractions of just a few percent (Fregeau et al. 2009). Such a small primordial binary fraction would be surprising since observations of young stars suggest that star formation yields binary fractions of order  $\sim 50\%$ . Clearly, our understanding of globular cluster evolution has changed considerably over the past few decades, and much of that change has been driven by numerical simulations.

Among computational tools for studying the dynamical evolution of star clusters, the Hénon Monte Carlo (MC) technique (Hénon 1971a,b) represents a balanced compromise between exactness and speed. The MC method allows for a star-by-star realization of the cluster, with its  $N$  mass shells representing the  $N$  stellar objects in the cluster (either single or binary stars). It assumes, most importantly, spherical symmetry and diffusive two-body relaxation, allowing time integration on a relaxation timescale, and a computational cost that scales as  $N \log N$ . We have developed our Hénon MC cluster evolution code (which we call CMC, for “Cluster Monte Carlo”) over the past decade (Joshi et al. 2000, 2001; Fregeau et al. 2003; Fregeau & Rasio 2007, henceforth Papers I, II, III, and IV, respectively). Since it allows for a star-by-star description of the cluster at each timestep, it is relatively easy to add physical processes beyond two-body relaxation to the code. We have previously added the effects of a Galactic tidal field, dynamical scattering interactions of binary star systems, and

physical collisions between stars. In this paper we describe the addition of stellar evolution of single and binary star systems. Many stars in a cluster evolve internally on a timescale shorter than the age of the cluster. At early times they may lose a substantial fraction of their mass via stellar winds. At later times they may evolve off the main sequence, changing their masses and radii (and hence collision cross section), and possibly receiving systemic velocity kicks when they become compact objects. Since the binding energy of binary stars is an important fuel source that can postpone the deep core collapse of star clusters, stellar evolution of binary systems directly affects their global evolution. Conversely, the properties of the cluster environment feed back on stellar evolution, modifying the evolutionary pathways of binary systems and the properties and numbers of interesting binary systems relative to the low-density Galactic field (e.g., X-ray binaries; Ivanova et al. 2006, 2008).

Previous cluster evolution studies that include stellar evolution have improved our understanding of the global evolution of clusters greatly, identifying several distinct stages of evolution. At early times, as the stars are forming and the most massive stars have already begun nuclear burning, the cluster loses mass through residual gas expulsion and stellar winds, resulting in cluster expansion during the first few Myr of evolution (Hurley et al. 2001, 2002). Shortly thereafter, if a runaway collision scenario is avoided (e.g., Freitag et al. 2006a), two-body relaxation dominates, resulting in a fairly long-lived (from a few to tens of Gyr) phase of core contraction. Once the core density becomes high enough for the energy generated in binary scattering interactions to balance the energy carried out of the core by two-body relaxation, a potentially *very* long-lived (up to tens of Hubble times or more) phase of “binary burning” ensues (e.g., Hurley 2007; Fregeau & Rasio 2007). Once the population of binaries is exhausted in the core, the cluster goes into deep core collapse. In the classical, point-mass limit, deep core collapse is arrested by the formation of a “three-body binary” and followed by a phase of gravothermal oscillations (Heggie & Hut 2003). However, three-body binary formation may be inhibited by stellar collisions in sufficiently young and massive clusters (Freitag et al. 2006b).

With the exception of a few recent simulations, most numerical studies that include stellar evolution have either been limited in the number of stars they can treat or have adopted a narrow initial mass function with very simplified stellar evolution recipes (e.g., Giersz 1998; Giersz & Spurzem 2000; Joshi et al. 2000, 2001; Fregeau et al. 2003; Fregeau & Rasio 2007). Stars in star clusters are born with a range of masses up to  $\sim 100 M_{\odot}$ , and down to at least the hydrogen-burning limit (e.g., Salpeter 1955; Miller & Scalo 1979; Kroupa 2001), so one should evolve the full spectrum of stellar masses as realistically as possible to properly treat the influence of stellar evolution on global cluster evolution. Emphasis has recently been placed on comparing observed properties of Galactic globular clusters with theoretical predictions. Comparison of observed cluster structural properties with theory (e.g., Hurley

2007; Fregeau & Rasio 2007) suggests that either an additional energy source is “puffing” up cluster cores (Mackey et al. 2008; Trenti et al. 2007; Chatterjee et al. 2008), or perhaps the clusters are not in the expected evolutionary states, namely binary-burning (Fregeau 2008). For example, recent  $N$ -body simulations by Hurley (2007) show that the core contraction phase can last a Hubble time, resulting in a cluster core radius that is larger than one would expect were the cluster in the binary burning phase. In these simulations, the core contraction phase is prolonged by mass loss from stellar evolution. Clearly, stellar evolution may be an important component in globular cluster evolution.

To more properly treat stellar evolution, we have recently coupled to CMC the stellar evolution recipes of Hurley et al. (2000, 2002, hereafter referred to as BSE). We choose BSE for ease of implementation, and for more direct comparisons with  $N$ -body calculations, which commonly use BSE for stellar evolution. In §2 we describe the implementation of stellar evolution in our code. In §3 we validate it by comparing with existing cluster evolution calculations in the literature. In §4 we demonstrate the importance of stellar evolution by comparing simulations that do not include it. In §5 we apply our newly updated code to the evolution of a large grid of cluster models, highlighting typical behavior and comparing with observations. Finally, in §6 we summarize and conclude.

## 2. Method

CMC treats a number of important physical processes, including two-body relaxation, the tidal effects of a host galaxy, strong binary-binary (BB) and binary-single (BS) scattering interactions, and direct physical collisions between stars (Paper IV). Here we describe the recent addition of BSE (Hurley et al. 2000, 2002) to treat stellar evolution of single and binary stars.

### 2.1. Stellar Evolution

For ease of implementation and for more direct comparisons with direct  $N$ -body we use the BSE stellar evolution routines, as described in detail in Hurley et al. (2000, 2002). For single stars, BSE comprises analytic functional fits to theoretically calculated stellar evolution tracks as a function of metallicity and mass. Binary star systems are treated using the same fitting formulae for each star, but with treatments of physics relevant to binaries, including stable and unstable mass transfer, common envelope evolution, magnetic braking, tidal coupling, and the effects of neutron star and black hole birth kicks. As described above,

CMC allows for a star-by-star description of the cluster at every timestep, allowing for the inclusion of additional physics. The stellar properties of binary and single stars are updated in step with dynamics via function calls to the BSE library. As described in detail in Papers I–IV, CMC uses a shared timestep which must be set as small as the smallest characteristic timescale for each physical process. We set the characteristic timescale for stellar evolution to the time for the cluster to lose a fraction 0.001 of its total mass. In this way, any cluster expansion from stellar evolutionary mass loss is properly resolved.

One aspect of our BSE implementation requires special mention, however. The evolution of high mass stars ( $\gtrsim 100 M_{\odot}$ ) is rather uncertain and can vary greatly depending on the wind mass loss prescription. These high mass stars are also quite rare and short lived, so observational constraints are limited. In BSE stars with mass  $> 100 M_{\odot}$  are evolved as if they were  $100 M_{\odot}$  stars. When their dynamical properties are returned from BSE, their original ( $> 100 M_{\odot}$ ) mass is returned.

## 2.2. Collisions

As described in Paper IV, collisions are treated in the sticky-sphere approximation, which was shown to be remarkably accurate for the velocity dispersions found in globular clusters (Freitag et al. 2006a,b). When two stars collide, their properties (e.g., stellar type and effective age) are set according to the BSE merger matrix and prescriptions as described in Hurley et al. (2002). In CMC this is implemented in the following simple way. The two stars are passed to BSE as a very tight, eccentric binary with nearly zero pericenter distance and evolved for a very short time until they merge. The properties of the merger product are then naturally set within BSE, and returned to CMC as a single star. BSE by default assumes full mixing of nuclear fuel during a collision involving MSSs. We adopt this same rejuvenation prescription for the simulations presented in this paper, but note that the amount of mixing in the collision product should depend on the details of the interaction parameters leading to the collision, as well as the evolutionary stages of the collision progenitors (e.g., Lombardi et al. 1995, 1996; Sills et al. 1997, 2001; Lombardi et al. 2002). In fact, it is found using detailed SPH calculations that the amount of mixing as a result of a collision may be minimal, especially for collisions involving evolved stars (Lombardi et al. 1995, 1996).

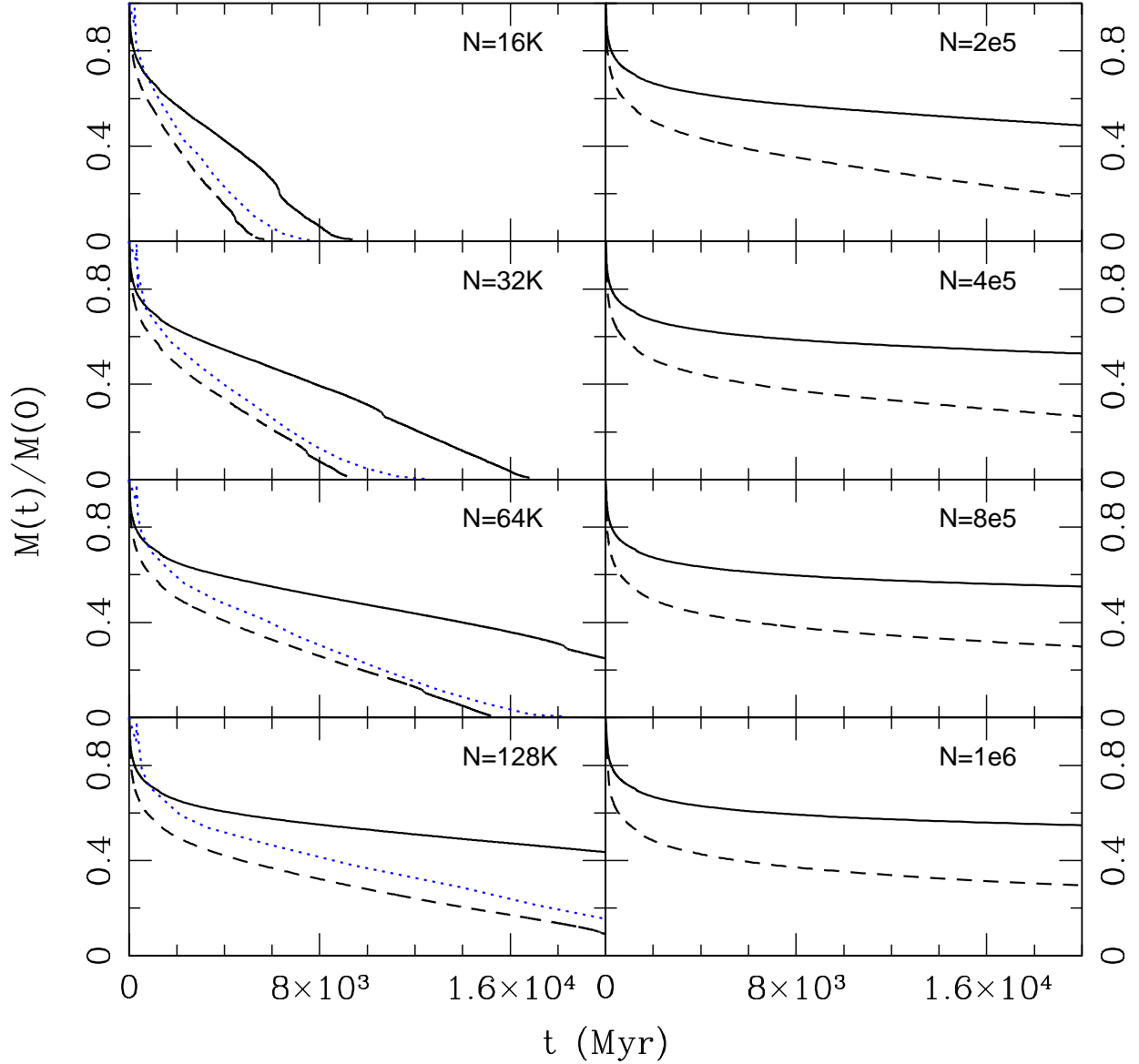


Fig. 1.— Evolution of the total cluster mass for clusters with various initial numbers of stars and masses. In each case a Galactocentric distance  $r_{GC} = 8.5$  kpc and a standard Galactic tidal field are assumed. The initial number of stars ( $N$ ) is noted in each panel. The solid black line and the dashed black line in each panel show CMC results with the apocenter criterion and energy criterion, respectively. The dotted blue line in the first four panels show the NBODY4 results for the same initial clusters for comparison. The NBODY4 data is taken from the simulations described in Baumgardt & Makino (2003). Similar simulations using NBODY4 do not exist for a higher  $N$ . In each case the energy criterion loses mass at a faster rate than the apocenter criterion. When available, the results using the energy criterion agree better with the direct  $N$ -body results.

### 2.3. Tidal Truncation Treatment

Globular clusters are not isolated systems, but are in fact subject to the tidal field of their host galaxy. The assumption of spherical symmetry inherent in MC codes like CMC does not allow for a direct calculation of stellar loss at the tear-drop shaped tidal boundary. Instead, MC codes employ an effective tidal mass loss criterion that attempts to match the tidal mass loss found in direct  $N$ -body simulations. Since stars are lost from the tidal boundary on a dynamical timescale and MC codes operate on the (much longer) relaxation timescale, the appropriate effective criterion is not obvious. There have been two main suggestions in the literature for the appropriate tidal truncation criterion. Perhaps the most natural is to immediately strip any star whose apocenter ( $r_a$ ) lies outside the Roche lobe radius of the cluster (which we call the tidal radius,  $r_t$ ):

$$r_a > r_t. \quad (1)$$

This “apocenter criterion” has been used exclusively in CMC previously (Papers I–IV). Earlier, in the absence of large- $N$  direct  $N$ -body simulations, comparisons were made with 2-D Fokker-Plank models and the apocenter criterion showed excellent agreement (for details see Papers I and II).

Another simple criterion is the “energy criterion,” in which any star with a specific orbital energy above some critical energy is immediately stripped:

$$E_{\text{orb}} > 1.5\phi_t, \quad (2)$$

where  $\phi_t$  is the cluster potential at the tidal radius (Spitzer 1987). However, a stellar orbit that instantaneously satisfies the above criterion may still remain bound if it is scattered back to a lower energy orbit before it can escape. To account for this effect a less obvious but empirically validated correction factor to the energy criterion above is suggested by Giersz et al. (2008):

$$E_{\text{orb}} > \alpha\phi_t, \quad (3)$$

where  $\alpha$  is an  $N$ -dependent parameter given by

$$\alpha = 1.5 - 3 \left[ \frac{\ln(\gamma N)}{N} \right]^{1/4}. \quad (4)$$

We have re-examined and tested these two criteria (Equations 1 and 3) for tidal stellar loss to determine which one agrees better with the latest results from direct  $N$ -body simulations. Baumgardt & Makino (2003) study in detail the tidal dissolution timescales of a cluster in a tidal field varying the initial number of stars and the initial mass of the cluster.

We have repeated a large subset of this extensive study of tidal disruption using CMC with both tidal truncation criteria, and compared the results.

We followed the exact same prescription for setting up the initial conditions of the clusters as described in Baumgardt & Makino (2003). Each cluster in this set of runs is assumed to have a circular orbit around the Galactic center with radius 8.5 kpc. The Galactocentric circular velocity  $V_G$  is assumed to be 220 km/s. The initial position and velocity of each star of the cluster is chosen from a King model distribution function with central concentration parameter  $W_0 = 7$ . The initial masses of the stars are chosen according to the Kroupa 2001 mass function in the range  $0.1 - 15 M_\odot$ . We vary the initial number of stars in the clusters between 16000 and  $10^6$ . There are no primordial binaries in these simulations.

Figure 1 shows the evolution of the bound mass in a cluster in the standard Galactic tidal field as described above. We find that the energy criterion results agree better with the direct  $N$ -body results, when available from Baumgardt & Makino (2003). The agreement is much poorer when using the apocenter criterion. For example, for the direct  $N$ -body run with initial  $N = 64K$ , the time when the cluster loses 80% of its initial mass is  $\approx 11$  Gyr. Using CMC with the energy criterion this value is  $\approx 10$  Gyr, whereas, with the apocenter criterion the same cluster does not lose 80% of its initial mass within 20 Gyr, the integration stopping time.

Since the energy criterion gives a significantly better agreement with existing direct  $N$ -body results (Figure 1; see also more detailed comparisons in §3), we adopt the energy criterion here, in contrast to what was used in our earlier works (Papers II – IV), unless otherwise mentioned.

One should note, however, that the cluster mass range where direct  $N$ -body results are available is not representative of the actual GGC population. Since no direct  $N$ -body results exist for more massive clusters, it is not possible at present to determine which approximation is more accurate for larger  $N$ .

The two criteria above are treated as initial options in CMC and either one can be selected at the beginning of a simulation. At each timestep, the amount of mass lost is calculated using the chosen criterion in an iterative way to obtain the bound mass (see Paper II for details).



### 3. Comparison with direct $N$ -body Results

In this section we validate our treatment of stellar evolution by comparing with results from previously published studies using the popular direct  $N$ -body code NBODY4 (Aarseth 2003). Since the direct  $N$ -body simulations employ the least degree of assumptions, we tend to trust them more for validation purposes.

One of the biggest simulations treating all relevant physical effects including primordial binaries and stellar evolution was performed by Hurley et al. (2007); Hurley (2007). In particular they studied the evolution of the core properties, binary number fractions in the core as well as in the full cluster, and the evolution of the bound number of stars. Since both these works present data from a common set of simulations we henceforth collectively call them Hurley07.

#### 3.1. Initial Conditions

We choose from Hurley07 the simulations with a number  $N_i = 10^5$  initial objects (the largest initial  $N_i$  in their set of simulations), with primordial binary fractions  $f_b = 5\%$  and  $f_b = 10\%$  (their K100-5 and K100-10 models, respectively). Throughout this work we count binary center of mass as one object. Thus a cluster with  $N_i = 10^5$  and  $f_{b,i} = 5\%$  initially has 95000 single stars and 5000 binaries. We simulate clusters with exactly the same initial conditions using CMC. The initial stellar positions and velocities are chosen from a virialized Plummer sphere. The stellar masses are chosen from the IMF presented in Kroupa et al. (1991, henceforth K91) in the range  $0.1 - 50 M_\odot$ . Metallicity is fixed at  $z = 0.001$ . Each cluster has an initial virial radius  $r_v = 8.5$  pc which corresponds to a roche-filling cluster with tidal radius  $r_t \sim 50$  pc, consistent with the standard Galactic tidal field with a Galactic rotation speed 220 km/s at a Galactocentric distance 8.5 kpc. The companion mass in each binary is chosen from a uniform distribution in mass ratio in the range  $0.1 - m_p M_\odot$ , where,  $m_p$  is the primary mass. The binary period is drawn from a distribution flat in logarithmic intervals in the semi-major axes (Eggleton et al. 1989) and the eccentricities are thermal following Hurley07. We call these simulations `hcn1e5b5` and `hcn1e5b10`, respectively (Table 1).

#### 3.2. Comparison of Results

For the global evolution of a dense cluster the evolution of the core is extremely important since throughout the evolution the global properties of the cluster are determined

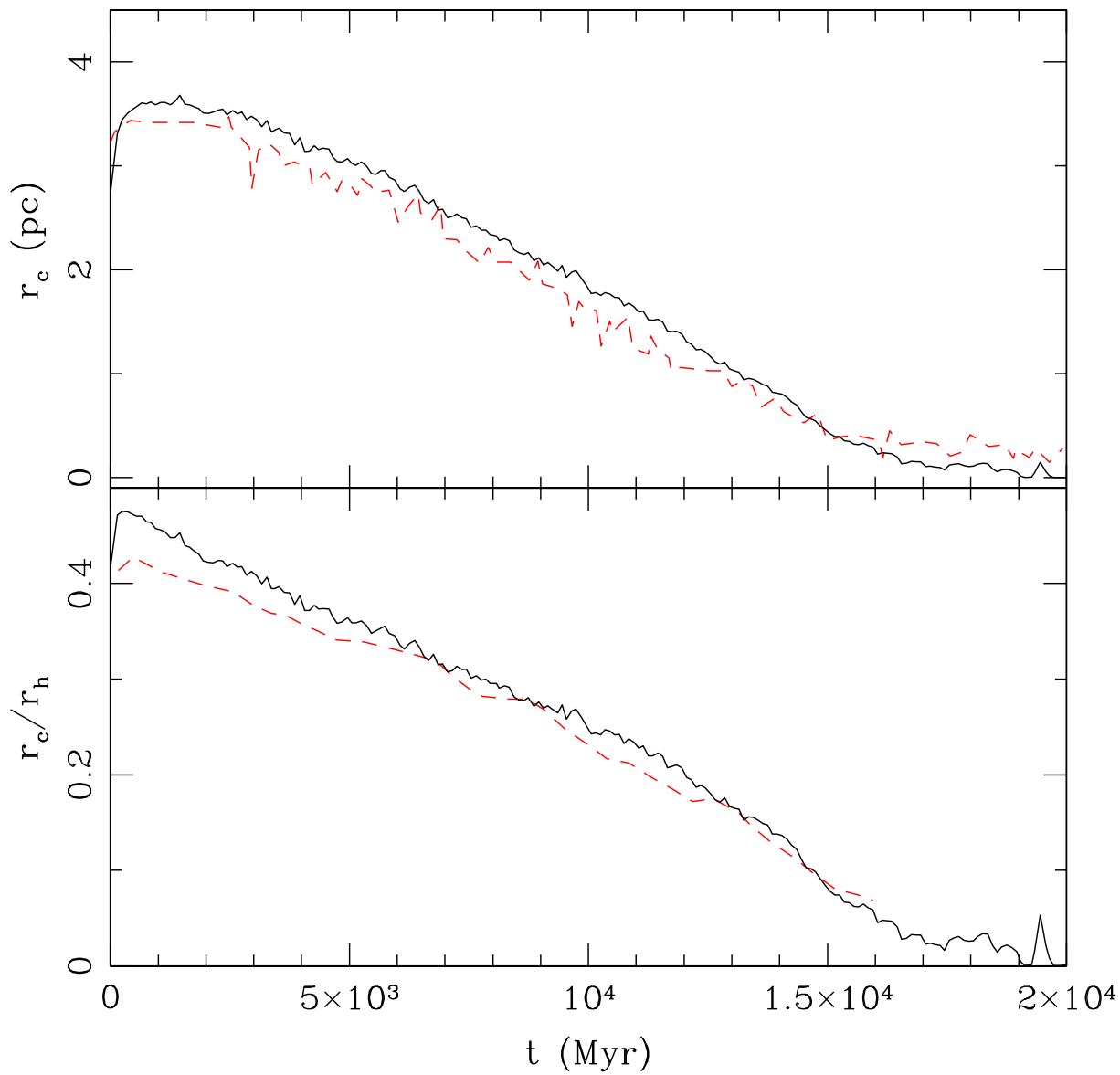


Fig. 2.— Evolution of  $r_c$  (top) and  $r_c/r_h$  (bottom). The solid black lines show results from simulation using CMC and the red dashed lines show results from Hurley07. All data from Hurley07 used for comparison in this work are extracted using ADS’s Dexter data extraction applet (Demleitner et al. 2001).

by the balance of energy in and out of the core. The core radius ( $r_c$ ) is also one of the most easily observable structural properties of a cluster. Moreover, the properties and the evolution of  $r_c$  is one of the easiest theoretical way to characterize the distinct phases of a cluster’s evolution. Thus a basic test for the validity of a cluster simulation is to compare the evolution of the core radius ( $r_c$ ) and the ratio of the core to half mass radius ( $r_c/r_h$ ).

Note that for all our simulated clusters in this work  $r_c$  is the density-weighted core radius (Casertano & Hut 1985) commonly used in  $N$ -body simulations, unless otherwise specified. This is not a directly observable quantity and can differ from the observed  $r_c$  by a factor of a few (Hurley 2007).

Figure 2 shows the evolution of  $r_c$  for run **hcn1e5b5** (Table 1) and K100-5 in Hurley07. The scale-free quantity  $r_c/r_h$  is also plotted for each run. The core radius expands due to stellar evolution mass loss during the first  $\sim 2 \times 10^2$  Myr. The core then contracts at a steady rate till a little after  $\sim 1.5 \times 10^4$  Myr. The core radius then attains a relatively steadier value as the cluster reaches the binary-burning phase (e.g. Fregeau & Rasio 2007). All these qualitatively different phases of the evolution of a cluster is reproduced using CMC with excellent agreement.

One of the key results of Hurley07 is that the overall binary fraction ( $f_b$ ) remains close to the primordial value throughout the evolution of the cluster (also see Fregeau et al. 2009). This result has immense observational significance. In practice only the present day properties of a cluster are observed. This result from Hurley07 indicates that if a present day binary fraction of the cluster close to  $r_h$  can be observed the primordial hard  $f_b$  should have been close to this observed value. Figure 3 shows the evolution of the core ( $f_{b,c}$ ) and the overall  $f_b$  from CMC simulation **hcn1e5b5** and direct  $N$ -body simulation presented in Hurley07. Binaries preferentially sink to the center due to mass segregation and the single stars typically get tidally disrupted from the tidal boundary. These two effects compete with each other—the first reduces and the second increases  $f_b$  outside the core. For the simulated cluster these two effects more or less balance each other. For the simulated cluster

Table 1. Initial conditions for comparison runs with Hurley07

Name	N	M ( $10^4 M_\odot$ )	Profile	IMF	$r_t$ (pc)	$r_v$ (pc)	$f_b$
hcn1e5b5	$10^5$	5	Plummer	K91 <sup>a</sup> [0.1, 50] $M_\odot$	51	8.5	0.05
hcn1e5b10	$10^5$	5	Plummer	K91 [0.1, 50] $M_\odot$	51	8.5	0.1

<sup>a</sup>Kroupa mass function as described in Kroupa et al. (1991).

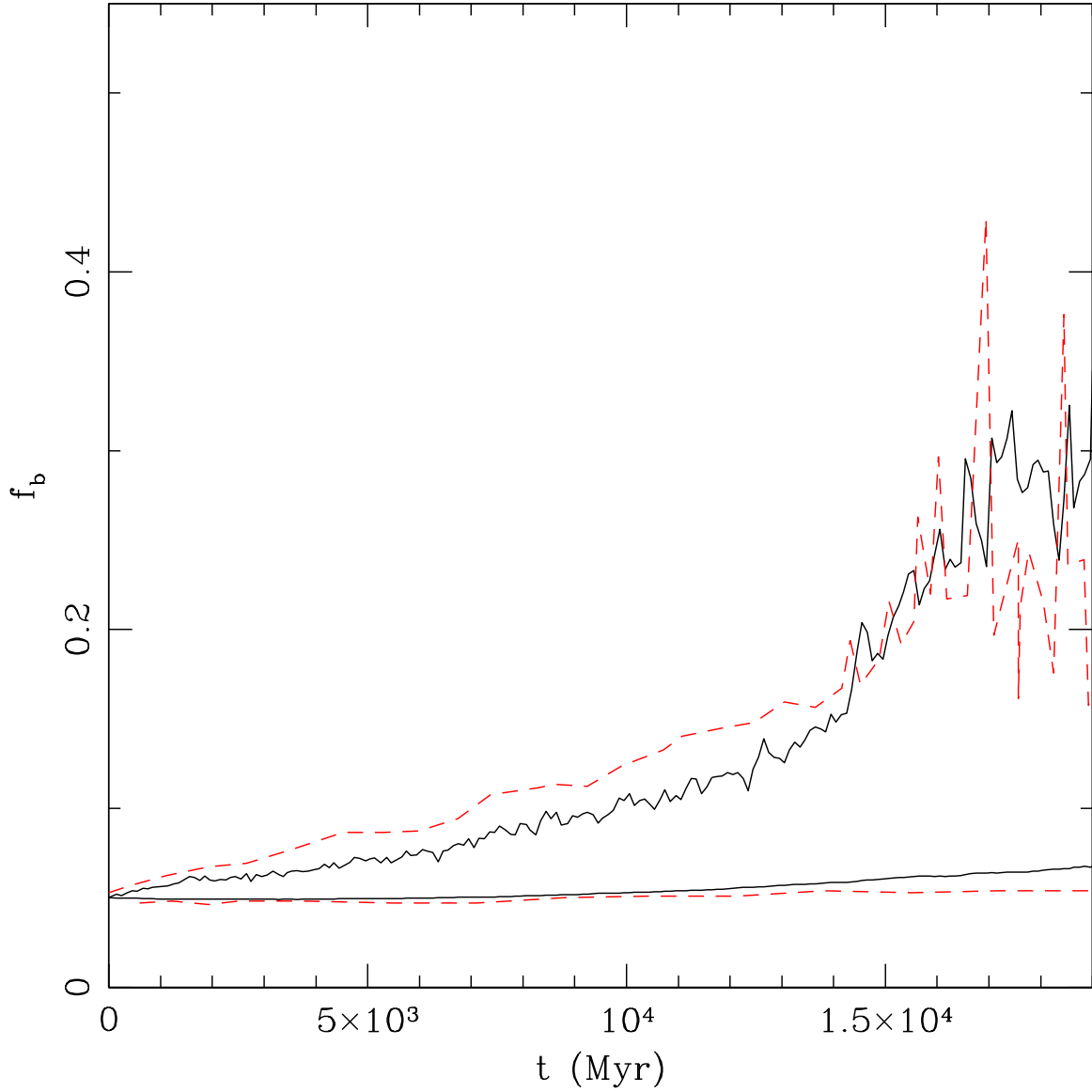


Fig. 3.— Comparison of evolution of the core and the overall binary fraction. Dashed red lines show results from Hurley et al. (2007, their K100-5 run). Solid black lines show results from CMC run using the exact same initial cluster parameters. In both sets the top line show the binary fraction within the core, and the bottom line show that for the whole cluster.

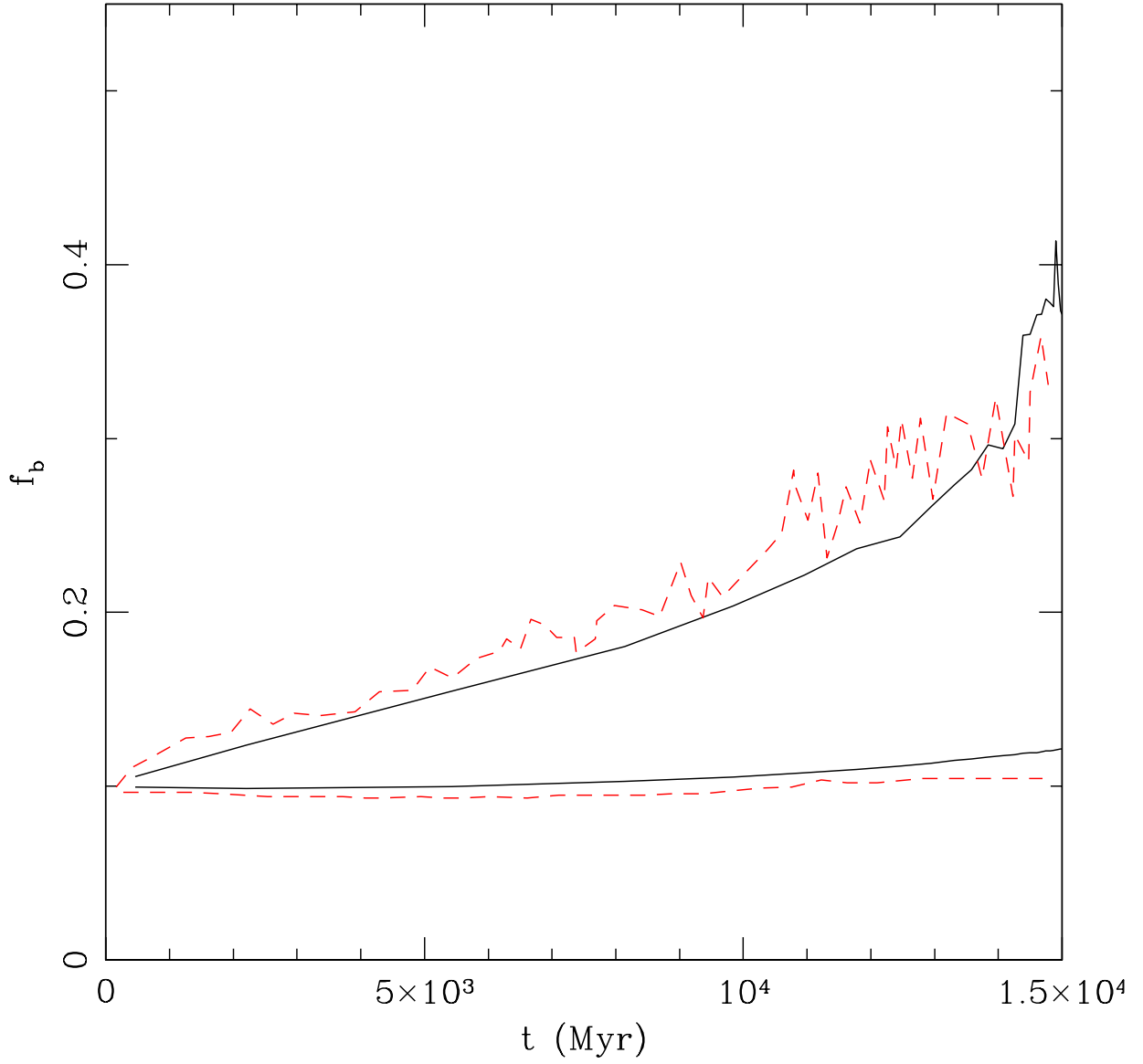


Fig. 4.— Same as Figure 3, using results from simulation hcn1e5b10. The CMC results are compared with the K100-10 simulation of Hurley07.

we reproduce the results presented in Hurley07 and verify that the overall  $f_b$  remains close to the primordial value whereas  $f_{b,c}$  increases over time. Similar results are found for the simulation `hcn1e5b10` (Figure 4).

We now focus on the evolution of the number of binaries in the core ( $N_{b,c}$ ). The evolution of the total number of core binaries is interesting for various reasons. The formation rates of interesting stellar objects such as X-ray binaries and blue straggler stars and their properties are directly dependent on  $N_{b,c}$ , motivating many detailed studies focusing on the evolution of  $N_{b,c}$  (e.g. Hurley et al. 2002; Ivanova et al. 2005, 2006, 2008; Fregeau et al. 2009). On one hand the core binary number ( $N_{b,c}$ ) increases due to mass segregation. On the other hand strong interactions involving binary-single (BS) and binary-binary (BB) encounters can lead to direct physical collisions or destruction of soft binaries and reduce  $N_{b,c}$ . In addition, binary stellar evolution can destroy binaries via evolution-driven mergers and disruptions. Since the evolution of  $N_{b,c}$  is dependent on these competing effects it is not simple to predict its evolution a-priori. Figure 5 shows the evolution of the number of core binaries ( $N_{b,c}$ ) for CMC run `hcn1e5b5` and direct  $N$ -body run K100-5 from Hurley07 for comparison. The evolution of  $N_{b,c}$  is reproduced exactly within the numerical fluctuations of the simulations. Over time the number of core binaries ( $N_{b,c}$ ) decreases.

It is also interesting to study the number fraction of binaries and single stars within the core compared to the global population. Although  $N_{b,c}$  decreases over time, due to mass segregation effects the number of single stars within  $r_c$  decreases more. Figure 6 shows the evolution of the number fractions of single stars ( $n_{s,c}$ ) and binaries ( $n_{b,c}$ ) within  $r_c$  for the same simulations as above. During the first  $\sim 10^4$  Myr  $n_{b,c}$  remains more or less constant whereas,  $n_{s,c}$  decreases by  $\sim 0.5$  of the initial  $n_{s,c}$  due to mass segregation effects. Followed by this phase BS/BB interactions as well as stellar evolution destroys core binaries decreasing  $n_{b,c}$ . However, throughout the evolution  $n_{b,c} > n_{s,c}$ . The combined effects of the above leads to the overall increase in  $f_{b,c}$  over time as seen in Figures 3 and 4. Note that although qualitatively CMC results and the direct  $N$ -body results agree, the agreement is not as excellent as the previous comparisons. For example, for the evolution of  $n_{b,c}$  there can be upto  $\approx 20\%$  difference in the absolute value depending on the age of the simulated cluster. The reason behind this larger difference compared to the excellent agreement for the evolution of  $N_{b,c}$  (Figure 5) originates from the approximations adopted in the tidal treatment in MC methods. The criterion based tidal removal of stars adopted in CMC loses stars from the tidal boundary at a relatively lower rate (Figure 7). Hence, at a given time the total number of bound single and binary stars in CMC are higher than those in Hurley07 making both  $n_{b,c}$  and  $n_{s,c}$  calculated using CMC systematically lower than the same calculated in Hurley07.

Another interesting result presented in Hurley07 is the evolution of the fraction of bina-

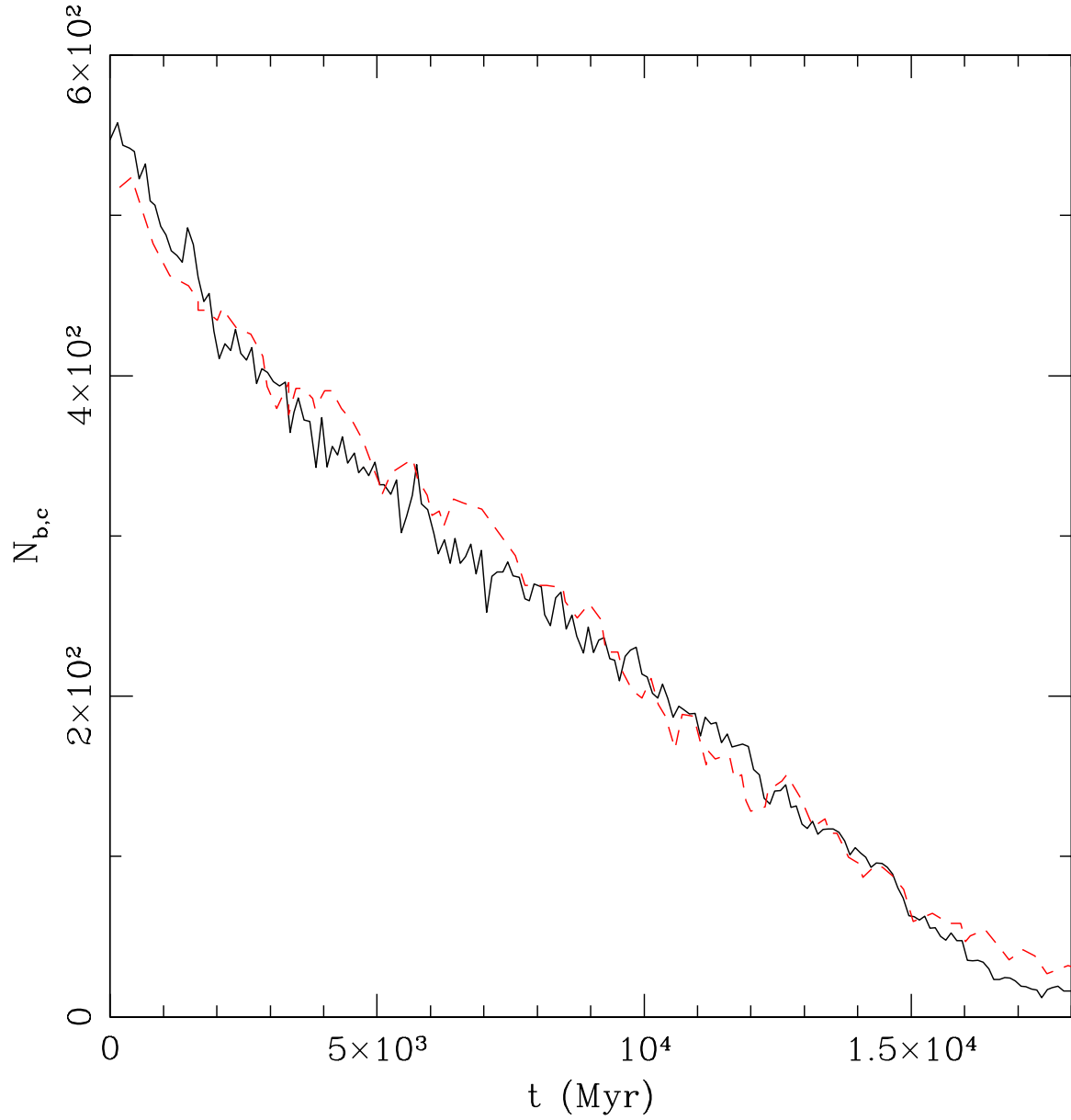


Fig. 5.— Evolution of number of binaries within  $r_c$  ( $N_{b,c}$ ). The solid black line shows the results from CMC run hcn1e5b5 and the red dashed line shows results from direct  $N$ -body run K100-5 from Hurley07.

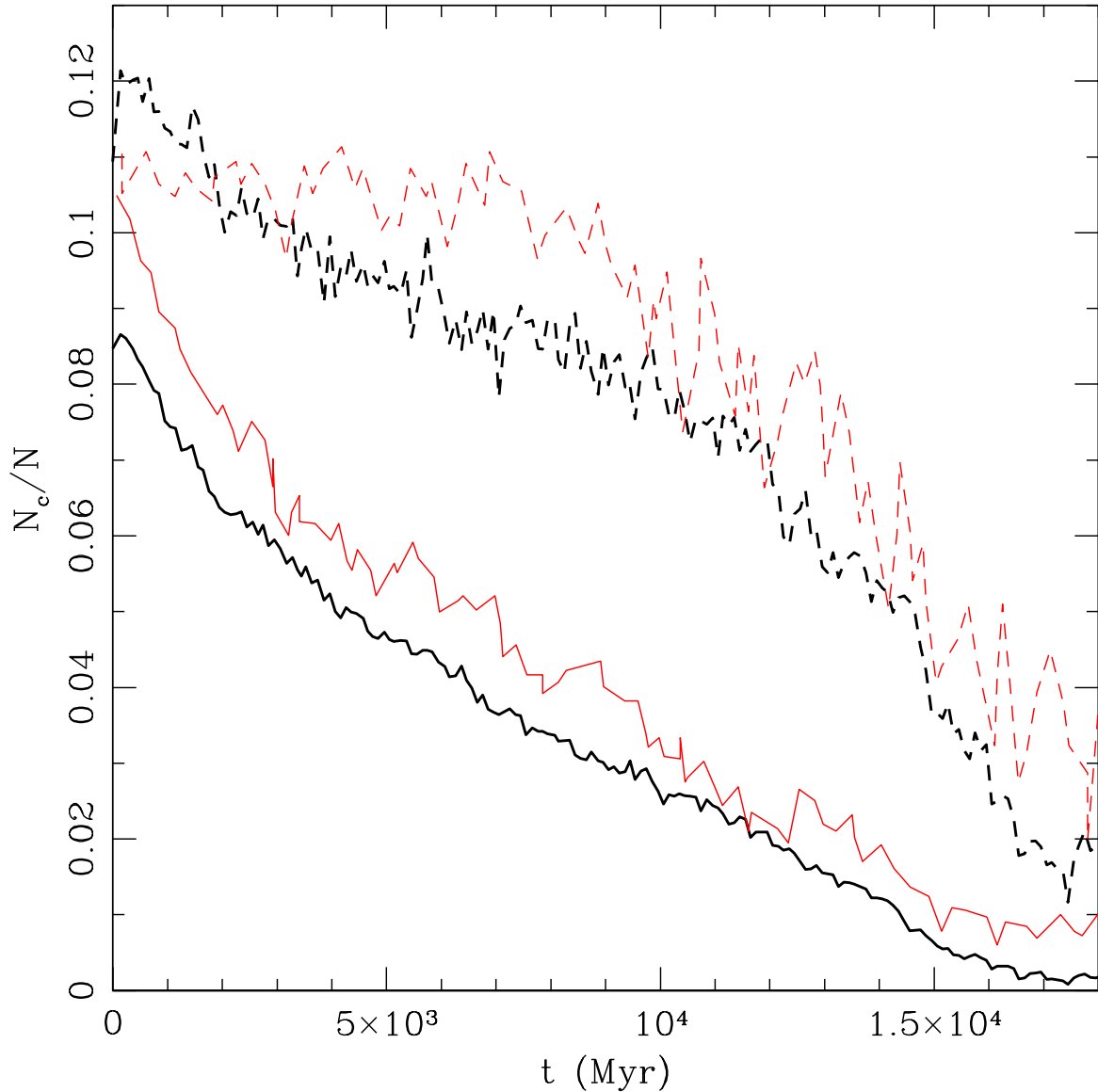


Fig. 6.— Evolution of the fraction (by numbers) of binary and single stars within the core. Thick black lines show the results from CMC. Thin red lines show the same from Hurley07. Solid and dashed lines show the number of singles and binaries within  $r_c$ , respectively. All numbers are normalized with the total number of that species at that time in the cluster (e.g.,  $N_{b,c}/N_b$  for the binaries). Both results clearly show the effects of mass segregation since throughout the evolution a higher fraction of binaries reside in the core.



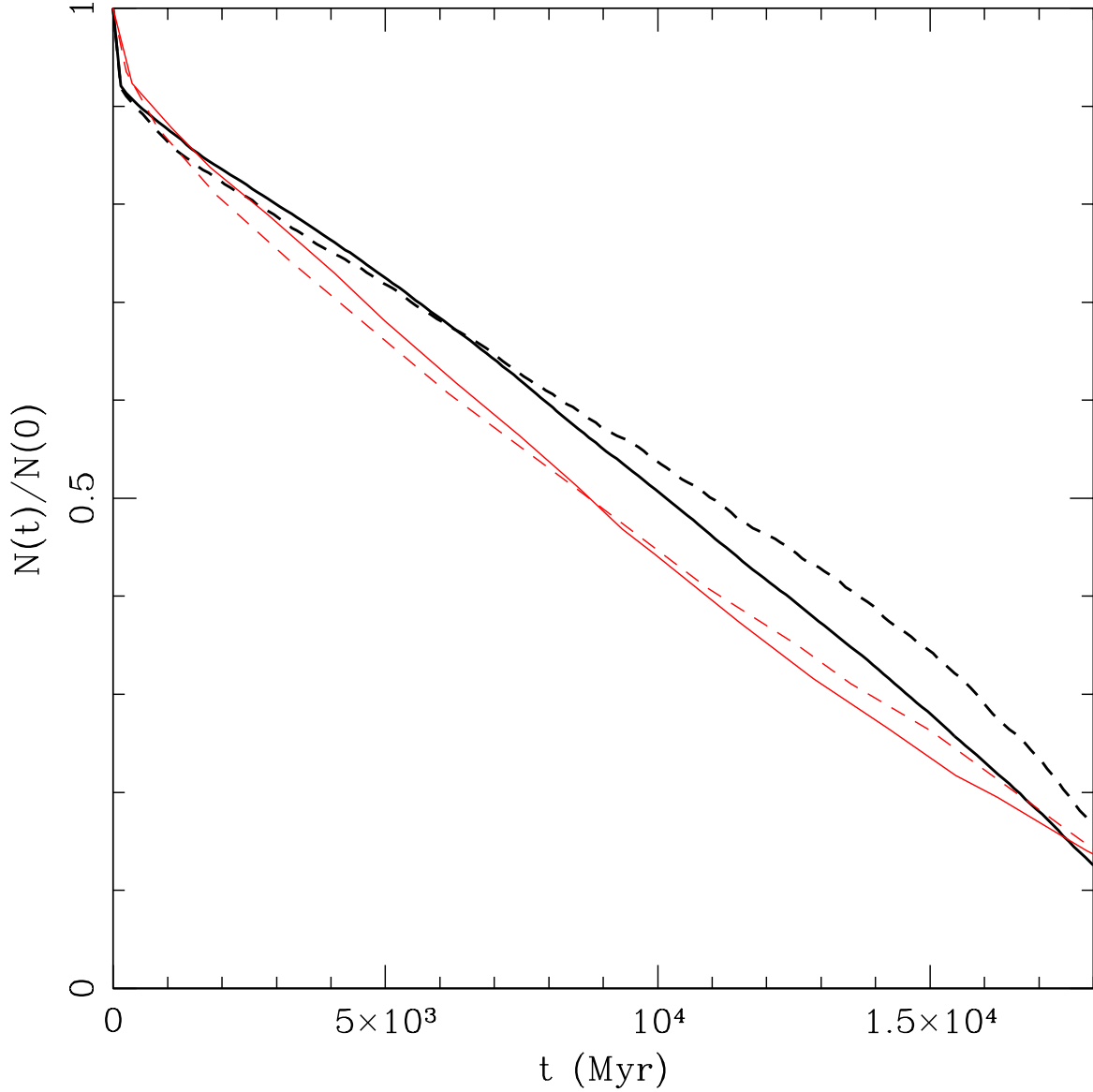


Fig. 7.— Comparison of the evolution of the number of single and binary stars that remain bound to the cluster. Thinner lines show results obtained from Hurley07. Thicker lines show results from CMC run using the same initial cluster parameters. Solid lines for both cases show the number of single stars bound at any given time. Dashed lines show the same for binaries. All numbers are normalized to the initial number of the same species (single or binary).

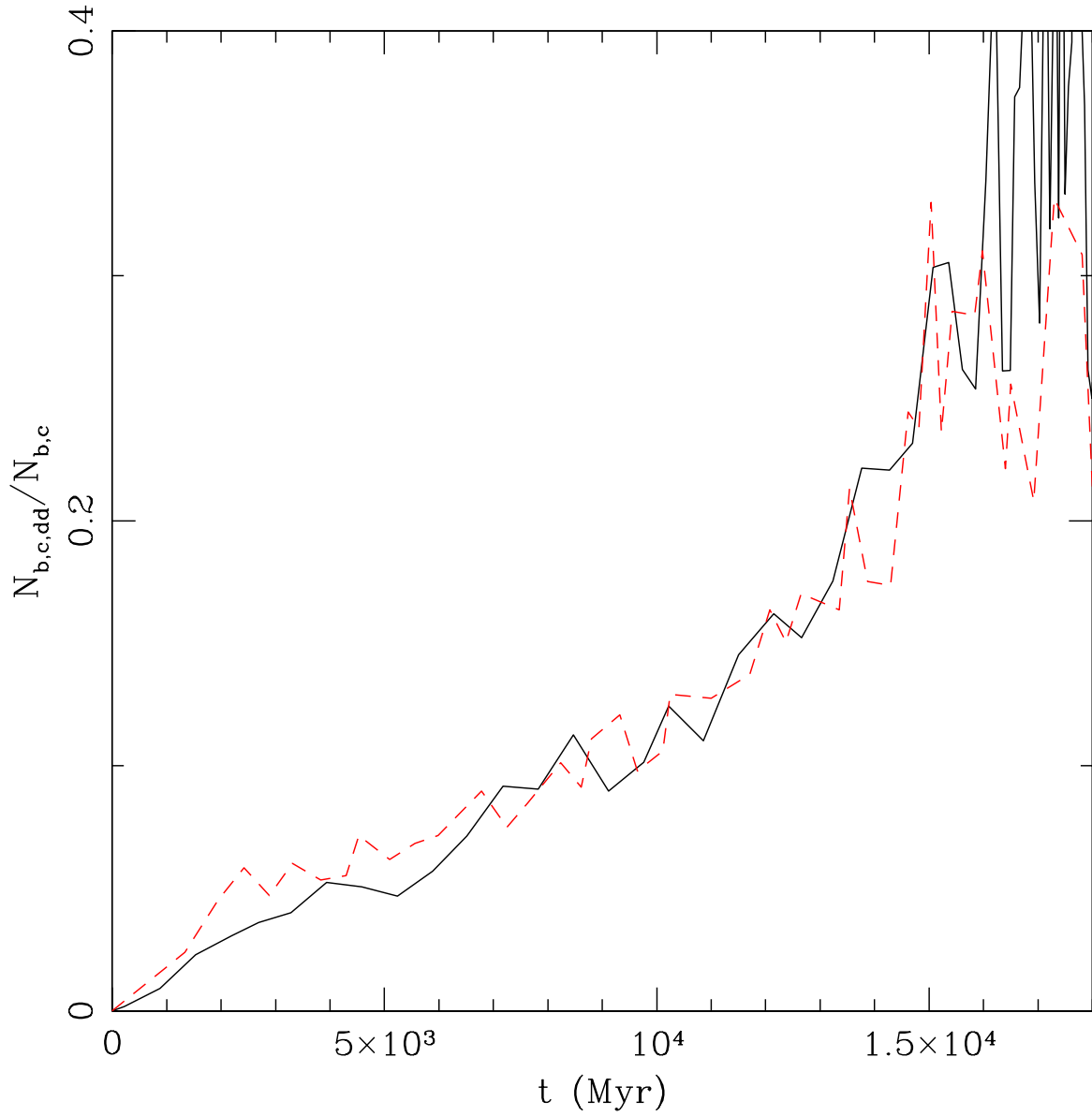


Fig. 8.— Evolution of the fraction of double-degenerate binaries within  $r_c$  with respect to all core binaries. Black solid and red dashed lines show results from CMC simulation and direct  $N$ -body simulation in Hurley07, respectively.

ries in the core where both components are compact objects. We call them double-degenerate binaries, following Hurley07. In Figure 8 we show the evolution of the fraction of double-degenerate core binaries for CMC run `hcn1e5b5` and direct  $N$ -body run K100-5. The fraction of double-degenerate binaries in the core depends on all physical processes in the cluster in a complicated way. Two-body relaxation drives mass segregation in the cluster determining the densities at different radial regions of the cluster as well as radius dependent velocity dispersion. This in turn directly affects the local BS/BB scattering cross-section at a given time consequently determining the survivability of a given binary at some radial position in the cluster and also the properties of the stellar members in a binary and the binary orbit. Changing the binary stellar properties and their orbital properties in turn changes the evolutionary pathways taken by the binary members and consequently compact object formation. Stellar evolution and dynamical effects thus in tandem affect the fraction of double-degenerate binaries in the core. The excellent agreement between CMC results with Hurley07 convinces us that not only the dynamical effects, but also the stellar evolution, and the rate of compact object formation, are modeled at least as accurately as in the direct  $N$ -body code NBODY4.

#### 4. Comparison With Simulations Without Stellar Evolution

We now examine the effects of stellar evolution on the evolution of the global observable properties of a GC, by performing comparisons to simulations without stellar evolution. The initial conditions for these simulations are summarized in Table 2.

Our most recent earlier paper, Paper IV, showed results from simulations without stellar evolution, but all other physical processes were included. In the absence of an implementation of full single and binary stellar evolution Paper IV restricted itself to simulations with a narrow range of masses in the IMF. We first compare the results with stellar evolution with a small subset of the previous runs from Paper IV without stellar evolution with the narrow

Table 2. Initial conditions for comparison runs including and leaving out stellar evolution

Name	N	Profile	IMF	$f_b$
kw4b03	$10^5$	King	K01 [0.1, 1.2] $M_\odot$	0.03
kw4b1	$10^5$	King	K01 [0.1, 1.2] $M_\odot$	0.1
kw4b3	$10^5$	King	K01 [0.1, 1.2] $M_\odot$	0.3
kw7b0	$5 \times 10^5$	King	K01 [0.1, 18.5] $M_\odot$	0
kw7b1	$5 \times 10^5$	King	K01 [0.1, 18.5] $M_\odot$	0.1

IMF as an example. Since this is for the purpose of comparison, we use the apocenter criterion (§2) for the tidal treatment to be consistent with Paper IV for these simulations.

For each of these simulations the initial stellar positions and velocities are chosen from a King profile with the concentration parameter  $W_0 = 4$ . For each simulation  $N_i = 10^5$ . The stellar IMF is chosen from the stellar MF presented in Kroupa (2001, henceforth K01). The initial binary fraction is varied between  $f_b = 0.03, 0.1$ , and  $0.3$ . The mass of each binary companion is chosen in the range  $0.1 - m_p$  from a uniform distribution in mass ratios. The binary periods are chosen from a distribution flat in logarithmic  $a$  intervals within physical limits, where, the hardest binary has  $a >$  the sum of the stellar radii of the companions and the softest binary is at the local hard-soft boundary. Binary eccentricities are thermal (e.g. Heggie & Hut 2003). For each of these initial conditions one simulation is done including stellar evolution and the other leaving it out.

We find that, even for the simulations with a small range of initial stellar masses, where the stellar evolution mass loss is not as severe as in a realistic cluster, for low  $f_b$  stellar evolution can influence the overall cluster evolution to a certain extent. Figure 9 shows the evolution of  $r_c/r_h$ . The results are shown for runs `kw4b0.03`, `0.1`, `0.3` (see Table 2). From top to bottom the primordial binary fractions  $f_b$  are 0.03, 0.1, 0.3, respectively. For  $f_b = 0.03$  even with the narrow mass range the two curves start diverging when the most massive stars (in this case  $1.2 M_\odot$ ) evolve off their MS and lose mass via compact object formation after  $\approx 3.4$  Gyr.

Binary interactions take place throughout the evolution of the cluster. As the initial  $f_b$  increases, energy available from super-elastic scattering of binaries becomes relatively more important compared to the energy produced from stellar evolution mass loss. Thus for this narrow range of masses as the binary fraction is increased, the difference between the results from simulations including stellar evolution and results without including stellar evolution reduces. For example, evolution of the cluster with initial  $f_b = 30\%$  is very similar with and without stellar evolution taken into account. The only difference is that at the quasi-steady binary-burning phase including stellar evolution makes  $r_c/r_h$  bigger by about 30%. In each of these clusters the central densities are not very high ( $\sim 10^4 M_\odot/\text{pc}^3$ ) so direct SS collisions are not dominant. When direct SS collisions are more important in a much denser cluster, this behavior may change (Chatterjee et al. 2008).

The difference in the evolution of the global properties depending on whether stellar evolution was included or not is, of course, a lot more dramatic when a more realistic IMF with a wider mass range is used. Here we use a King profile with central concentration parameter  $W_0 = 7$ . The IMF is according to the K01 stellar MF in the range  $0.1 - 18.5 M_\odot$ . Two such clusters are simulated one with no primordial binaries and the other with  $f_b = 0.1$ .

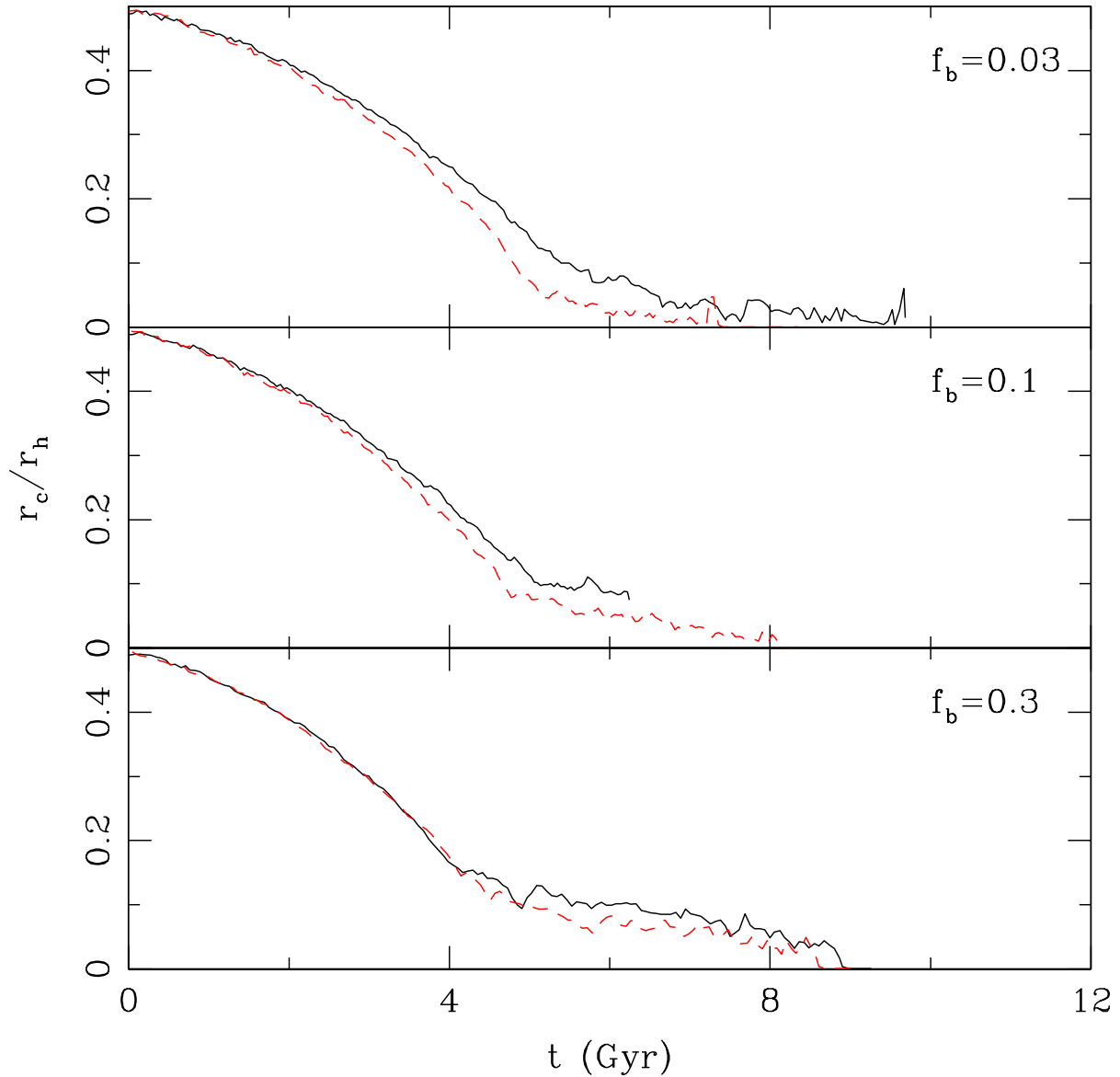


Fig. 9.— Comparison of the evolution of  $r_c/r_h$  with (solid black) and without (dashed red) stellar evolution, both using CMC. Results without stellar evolution were already presented in Paper IV. Each run starts with  $10^5$  objects. The velocities and positions of the objects are chosen from a King profile with an initial  $W_0 = 4$ . The masses are chosen from a Salpeter MF in the range  $0.2 - 1.2 M_\odot$ . From top to bottom the initial binary fractions are 0.03, 0.1, and 0.3.

Note the dramatic difference in the evolution of the simulated clusters. The evolution during the initial  $\sim 10^2$  Myr is dominated by the mass loss via stellar evolution of the high mass stars and compact object formation (Figure 11). This phase is clearly distinguished by the initial steep expansion of the cluster (Figure 10). This phase is followed by a slow contraction phase. In this phase, two-body relaxation drives the evolution. The high mass stars have already evolved off the MS and the stars remaining in the cluster are evolving at a much slower rate. The transition between the initial stellar evolution driven expansion and the slow contraction happens when the energy generation rate from stellar evolution mass loss becomes less than the outwards energy diffusion rate from the core due to relaxation. The cluster then keeps contracting until the central density increases so much that BS/BB interaction rates become high enough and the energy injected by the hard binaries (via super-elastic scattering) balances the energy diffusion rate from relaxation. The cluster then reaches the binary-burning phase. All these phases are clearly seen in Figure 10, bottom panel.

Even with this moderately broad range in mass, the clusters without stellar evolution contracts rapidly and are driven towards a quick collapse. If there are primordial binaries, the binary-burning phase starts relatively early ( $\sim 1$  Gyr, Figure 10). On the other hand, when stellar evolution is included, even without any primordial binaries the same cluster may still be in the slow contraction phase at Hubble time. For the cluster with primordial binaries in this case the binary-burning starts only after 11 Gyr (Figure 10).

## 5. Results for Realistic Galactic Globular Clusters

We have validated CMC by extensive comparisons with direct  $N$ -body results (§3). Moreover, we have shown the importance of including stellar evolution in cluster modeling including a realistic stellar IMF (§4). We now simulate a large grid of clusters with realistic initial conditions for 12 Gyr taking all physical processes into account, including primordial binaries and single and binary stellar evolution, and the full observed stellar mass range spanning three orders of magnitude. Our goal here is to simulate clusters with realistic initial conditions motivated from observations of young clusters (e.g., Scheepmaker et al. 2007) and find whether at a simulated cluster age of  $\approx 12$  Gyr, a typical age for the GGCs, the simulated clusters show similar observable properties (e.g.,  $r_c$ , and  $r_c/r_h$ ) as the observed population.

The proper initial conditions for the GGCs are uncertain, however. Moreover, it is hard to infer uniquely the initial conditions from the present day observed cluster properties since the observed cluster global properties as well as their galactic orbits can be

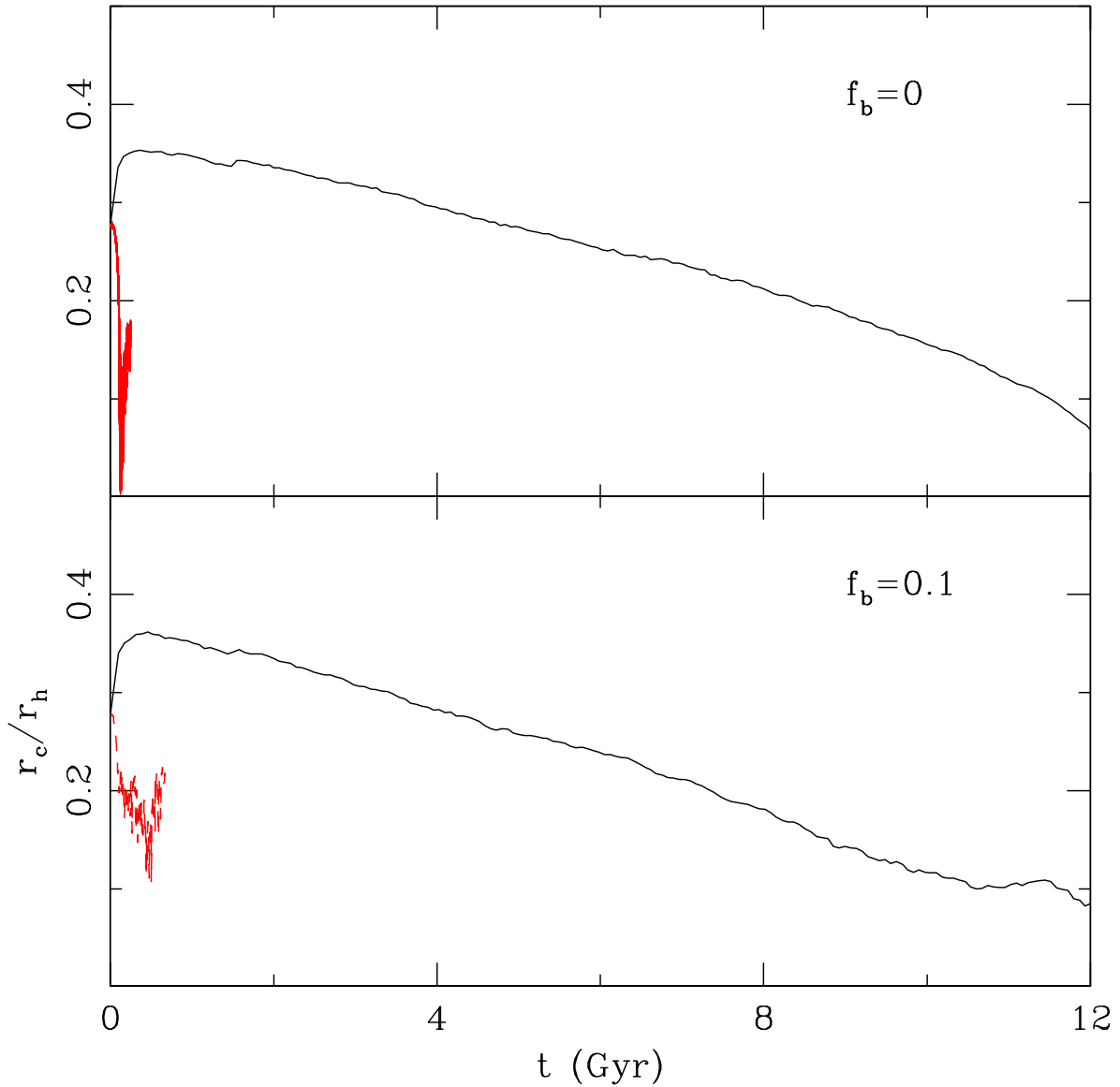


Fig. 10.— Comparison between two sets of simulations, all using CMC, but in one set stellar evolution is included and in the other it is not. Both panels show simulations with an initial King profile cluster with  $W_0 = 7$  and a Kroupa 2001 IMF in the range  $0.1 - 18.5 M_\odot$ . The top panel shows results with no primordial binaries. The bottom panel shows results with 0.1 initial  $f_b$ . For all simulations the initial number of objects is  $5 \times 10^5$ . On both panels dashed red lines are for simulations leaving out stellar evolution and solid black lines are for simulations including stellar evolution. A dramatic difference is clearly noticeable caused by stellar evolution mass loss.

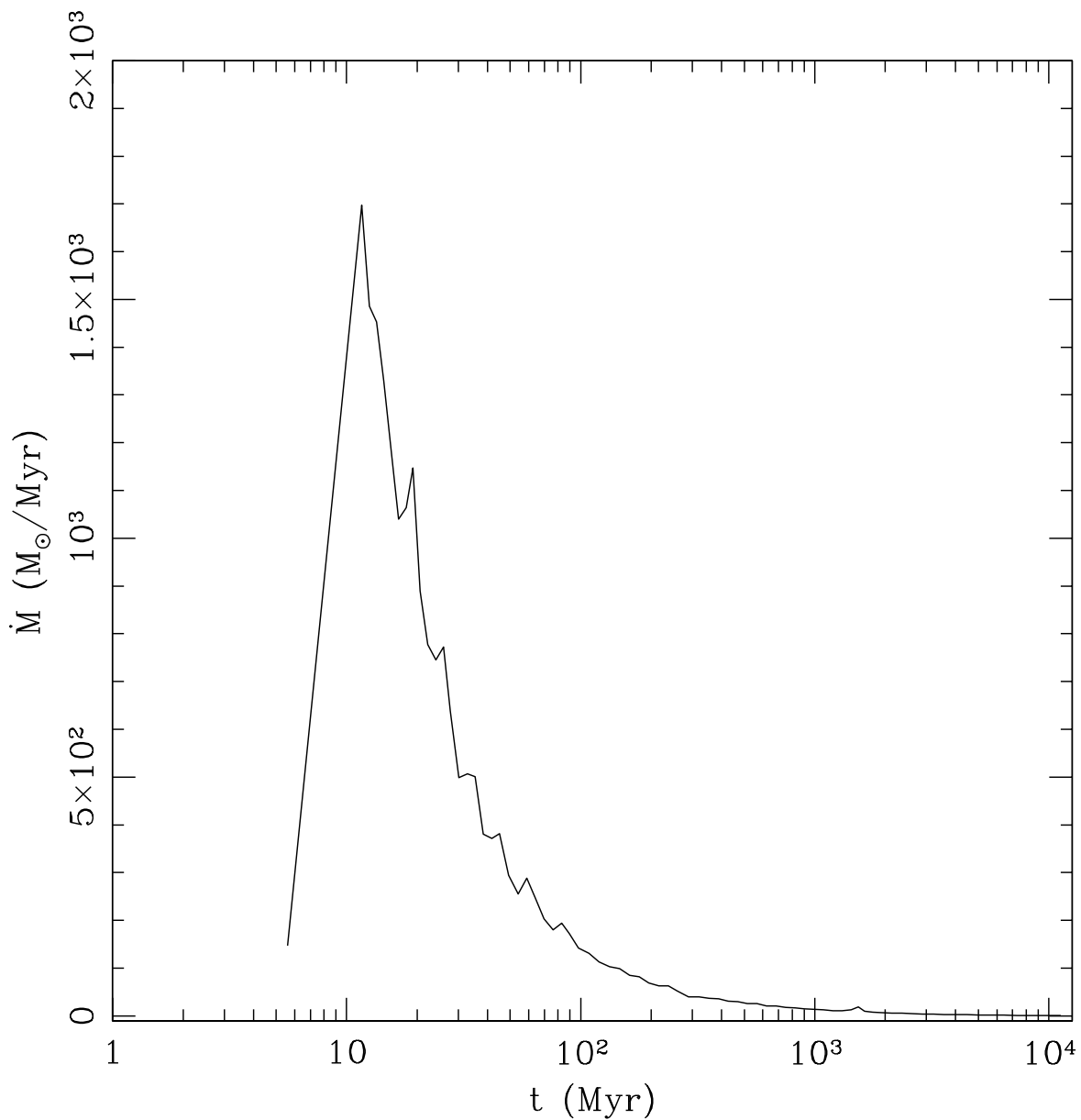


Fig. 11.— Rate of stellar evolution mass loss as a function of time. Within 10-100 Myr most of the mass is lost due to stellar evolution while high mass stars  $M_{\star} \gtrsim 5 M_{\odot}$  evolve off their MS. Followed by this initial phase the mass loss rate from winds and compact object formation is low.



quite uncertain (e.g., Heggie & Giersz 2008). Hence, rather than trying to create a detailed model for any particular cluster we compare the collective results of all our grid runs with the observed GGC properties as a whole. For comparison the GGC properties are extracted from the Harris Catalogue for GGCs (Harris 1996, and the references therein; also see <http://www.physics.mcmaster.ca/Globular.html>). When an observable is not reported in the catalogue for a cluster, we exclude that cluster from comparison. In the following subsections we explain the initial setup of the grid of simulations and present our results.

### 5.1. Initial Conditions

We simulate clusters with a large grid of initial conditions. All simulated clusters has a fixed initial virial radius  $r_v = 4$  pc (corresponds to an initial  $r_h \approx 3$  pc). Observations indicate that the effective radius of both young and old clusters are rather insensitive to the cluster mass, and metallicity (e.g. Ashman & Zepf 2001; Scheepmaker et al. 2007, 2009) and has a median value of  $\sim 3$  pc. In addition, observations of old massive LMC clusters, old GCs in NGC 5128, old clusters in M 51, as well as the GGCs indicate that the effective cluster radii show only a weak positive relation with the distance from the galactic center (Hodge 1962; Harris et al. 1984; Hesser et al. 1984; Mateo 1987; van den Bergh et al. 1991; Scheepmaker et al. 2007; Hwang & Lee 2008).

To restrict the huge parameter space to a certain extent we place all our simulated clusters in a circular orbit at a Galacto-centric distance of  $r_{GC} = 8.5$  kpc, where the Galactic field is not so strong that the tidal stellar loss dominates the cluster’s evolution. Choosing a circular orbit for the simulated clusters is a simplification, however, the results should still be valid for eccentric orbits with some effective pericenter distance of 8.5 kpc (e.g., Baumgardt & Makino 2003). The Galactic tidal field and consequently the initial  $r_t$  for the clusters are calculated using a Galactic rotation speed  $v_G = 220$  km/s following the standard practice.

For the set of runs we vary  $N_i$  between  $4 - 10 \times 10^5$ , the initial  $W_0$  for King models in the range  $4 - 7.5$ , and initial  $f_b$  between  $0 - 0.1$ . For each case we choose the stellar masses of the primaries from the MF presented in K01 in the range  $0.1 - 100 M_\odot$ . The masses of each binary companion is chosen from a uniform distribution of mass ratios in the range  $0.1 - m_p M_\odot$ .  $a$  for the binaries are chosen from a distribution flat in log within physical limits, namely physical contact of the components and the local hard-soft boundary. Although initially each binary is hard at its position it may not remain so during the evolution of the cluster. The cluster contracts under two-body relaxation and the velocity dispersion increases making initially hard binaries soft. Moreover, binaries sink to the core due to mass segregation

where the velocity dispersion is higher than the velocity dispersion for the binaries at  $t = 0$ . We include these soft binaries in our simulations. We let the cluster dynamics disrupt these binaries via BS/BB interactions. So at any instant of time soft binaries are allowed in the cluster as long as they have not been disrupted naturally via dynamical encounters yet. This is closer to reality and this strategy is adopted since soft binaries can act as an energy sink and can contribute to the overall cluster energetics significantly (Fregeau et al. 2009).

Each cluster is evolved for 12 Gyr including all physical processes— two body relaxation, stellar evolution, strong encounters like BB, BS, and SS collisions. For clusters that reach a deep-collapse phase, the CMC time steps become minuscule and the code grinds to a halt. We stop our simulations at that point for these clusters. Note that in reality, the deep collapse phase is halted via formation of the so called three-body binaries and the cluster enters into the gravo-thermal oscillation phase. Since in CMC we do not include the possibility of creating new binaries via three body encounters, we do not address this phase at this stage. However, this is not a serious limitation for this study since all simulated clusters that reach this phase within 12 Gyr had a primordial  $f_b = 0$ , which is not realistic (e.g., see most recently Davis et al. 2008) and simulated for academic interests only. None of the simulated clusters enter into the deep-collapse phase before  $\approx 9$  Gyr. The properties of all these grid simulations are summarized in Table 3.

## 5.2. Results

Here we present some basic observable properties of the simulated clusters and compare them with the same properties of the observed GGCs. For each of these comparison plots the evolution of a cluster property is shown with the distribution of the same property in the GGC population including all GGCs where observation of the concerned property exists. Since we restrict the galacto-centric distance of our simulated clusters for this study to be 8.5 kpc (§5.1) we also show the observed distribution of the GGCs with pericenter distances from the Galactic center within 7 – 10 kpc to be consistent in the comparisons. Note that the purpose for this comparison is simply to ensure that the simulated cluster properties agree well with the observed GGC properties. We do not intend to create a present day distribution for these properties since for that a probability distribution for the initial conditions is required, which is poorly constrained and beyond the scope of this study.

Note that for the observed GGCs only the sky projection of the characteristic radii such as  $r_c$  and  $r_h$  are known. Hence, in order to be consistent in our comparisons with the observed population we show the evolution of the 2D projections of  $r_c$ , and  $r_c/r_h$  for all simulated

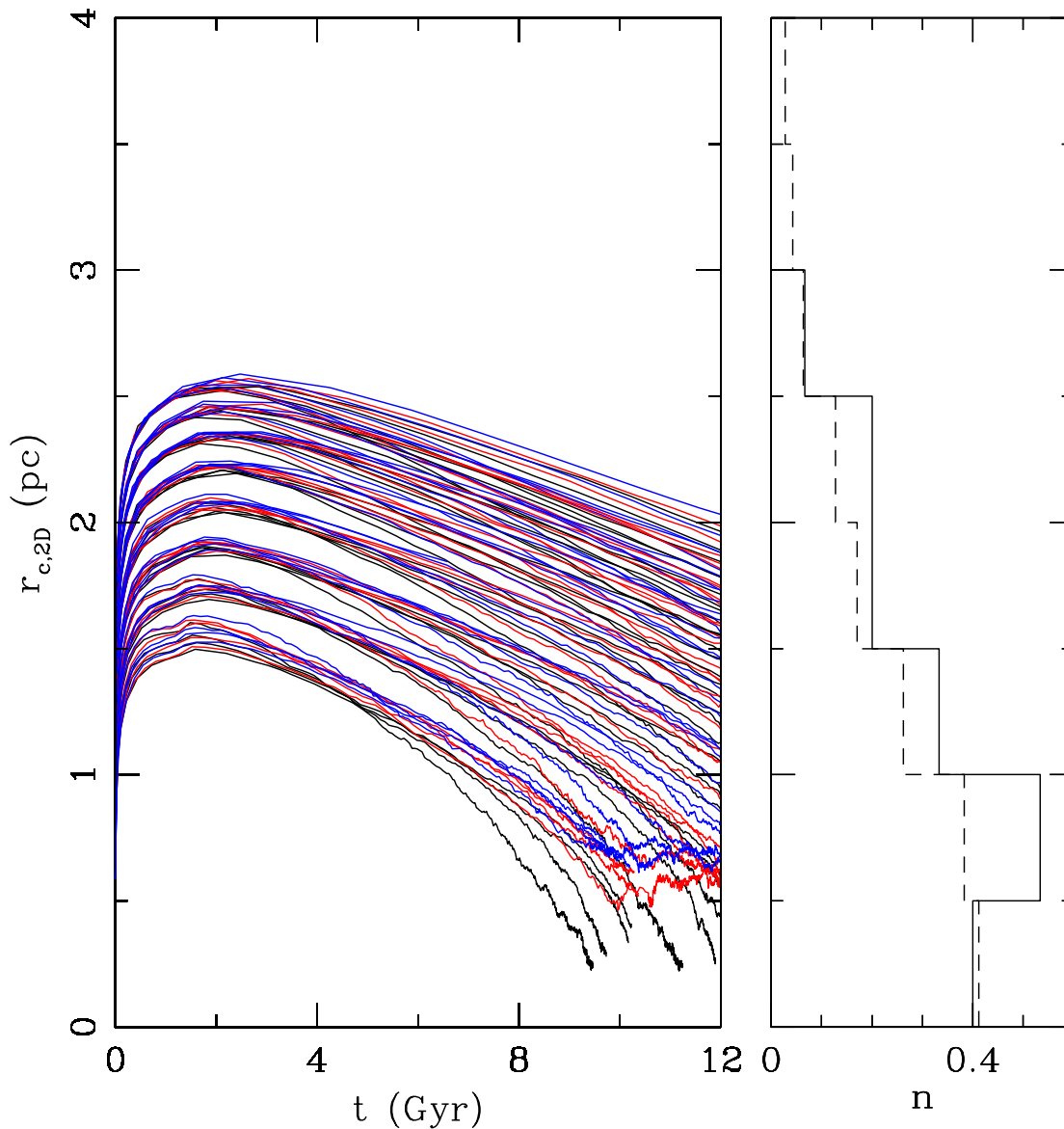


Fig. 12.— Evolution of the 2D projection of  $r_c$  for all simulated clusters. The black, red, and blue lines are for clusters with initial  $f_b = 0, 0.05,$  and  $0.1,$  respectively. A few (6) clusters with  $f_b = 0$  go into deep-collapse within a Hubble time. We stop integrations for those clusters when this phase is reached. The  $r_c$  values for the observed GGCs are also shown in histograms. The solid histogram is for GGCs with pericenter distances between  $7 - 10$  kpc. When the orbital eccentricities are unknown, a circular orbit is assumed. The dashed histogram is for all GGCs where a measurement for  $r_c$  exist.

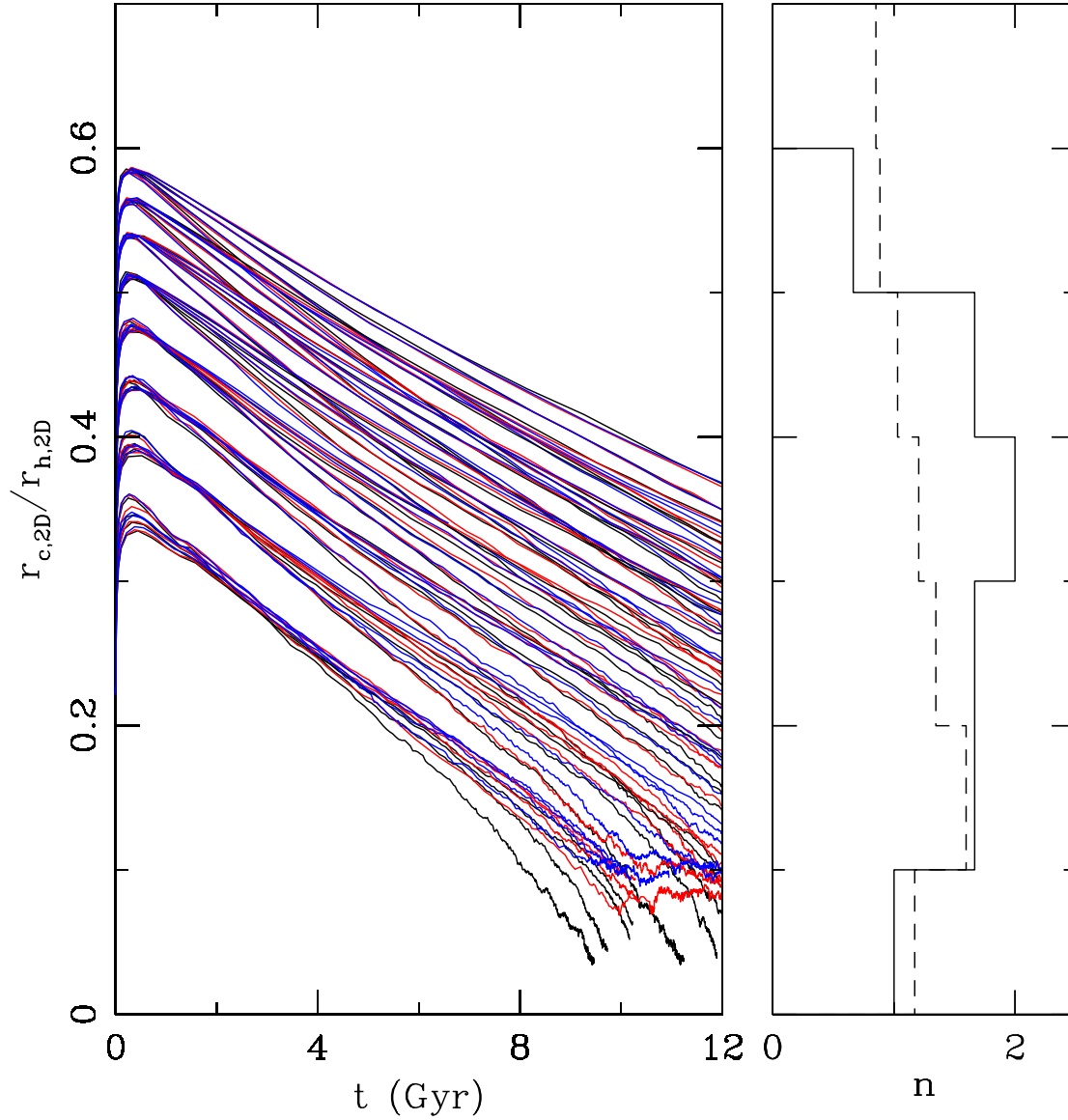


Fig. 13.— Same as Figure 12 for the ratio of the 2D projection of the  $r_c$  to the 2D projection of the  $r_h$  for all simulated clusters. The  $r_c/r_h$  values for the observed GGCs are also shown in histograms. The solid and the dashed histograms are from GGC populations selected as in Figure 12.

clusters (e.g., Figures 12 and 13). The sky projections for all simulated clusters are done assuming spherical symmetry. Both  $r_c$  as well as the  $r_c/r_h$  values of the simulated clusters agree well with the observed values in the GGC population producing values at 12 Gyr close to the peak of the observed distribution.

We should remind the readers, however, that these  $r_c$  and  $r_h$  values are not exactly the quantities observed directly. As mentioned before,  $r_c$  is the density-weighted core radius (Casertano & Hut 1985), related to a virial radius in the core, commonly used in  $N$ -body simulations, and can differ from an observed  $r_c$  by a factor of a few (Hurley 2007). Similarly, only the half-light radius is observed which may differ from the half-mass radius of a cluster. For example, for a typical simulated cluster **c1f3n4** the half light radius including all stars is 4.7 pc. If the giant stars are excluded (a common practice for observers) for the same cluster the half light radius is 4.1 pc. The theoretically calculated half mass radius for the same cluster at the same age is 7 pc.

Nevertheless, one should remember that without including stellar evolution the simulated  $r_c/r_h$  values including primordial binaries were found to be about an order of magnitude smaller than in the observed population (e.g., Paper IV, Vesperini & Chernoff 1994) and several studies proposed different additional energy generation mechanisms to explain the large observed  $r_c/r_h$  values (e.g. Trenti et al. 2007; Chatterjee et al. 2008; Fregeau 2008; Mackey et al. 2008). It is thus quite exciting to find such agreement simply by including stellar evolution in the simulations without the need for any fine tuning with the initial conditions or exotic scenarios.

To focus on the distinct evolutionary stages of the clusters we now choose three clusters from our large grid of simulations. These clusters are representative of clusters in three distinct end stages. Cluster **c1f3n4** is at the slow contraction phase at the integration stopping time and cluster age  $t_{cl} = 12$  Gyr. Cluster **c3f2n1** completes the slow contraction phase at  $t_{cl} \sim 10$  Gyr, reaches the binary-burning quasi-steady phase and remains in the binary-burning phase until the integration stopping time  $t_{cl} = 12$  Gyr. Cluster **c8f1n1** reaches the deep collapse phase at  $t_{cl} \approx 9$  Gyr (Figure 14). Integration is stopped after this stage is reached. As mentioned earlier, cluster **c8f1n1** has no primordial binaries and shown only as a limiting case for comparison. For each of the simulated clusters the three distinct phases of cluster evolution are clearly observed. All simulated clusters first expand due to stellar evolution mass loss during the first  $\sim 1$  Gyr. Followed by this initial expansion the clusters slowly contracts due to two-body relaxation. This slow contraction phase ends in the quasi-steady binary-burning phase for clusters with primordial binaries (Table 3 runs except **cif1ni**, where  $i \in [1, 4]$ ). Clusters without primordial binaries go into deep-collapse directly at the end of slow contraction.

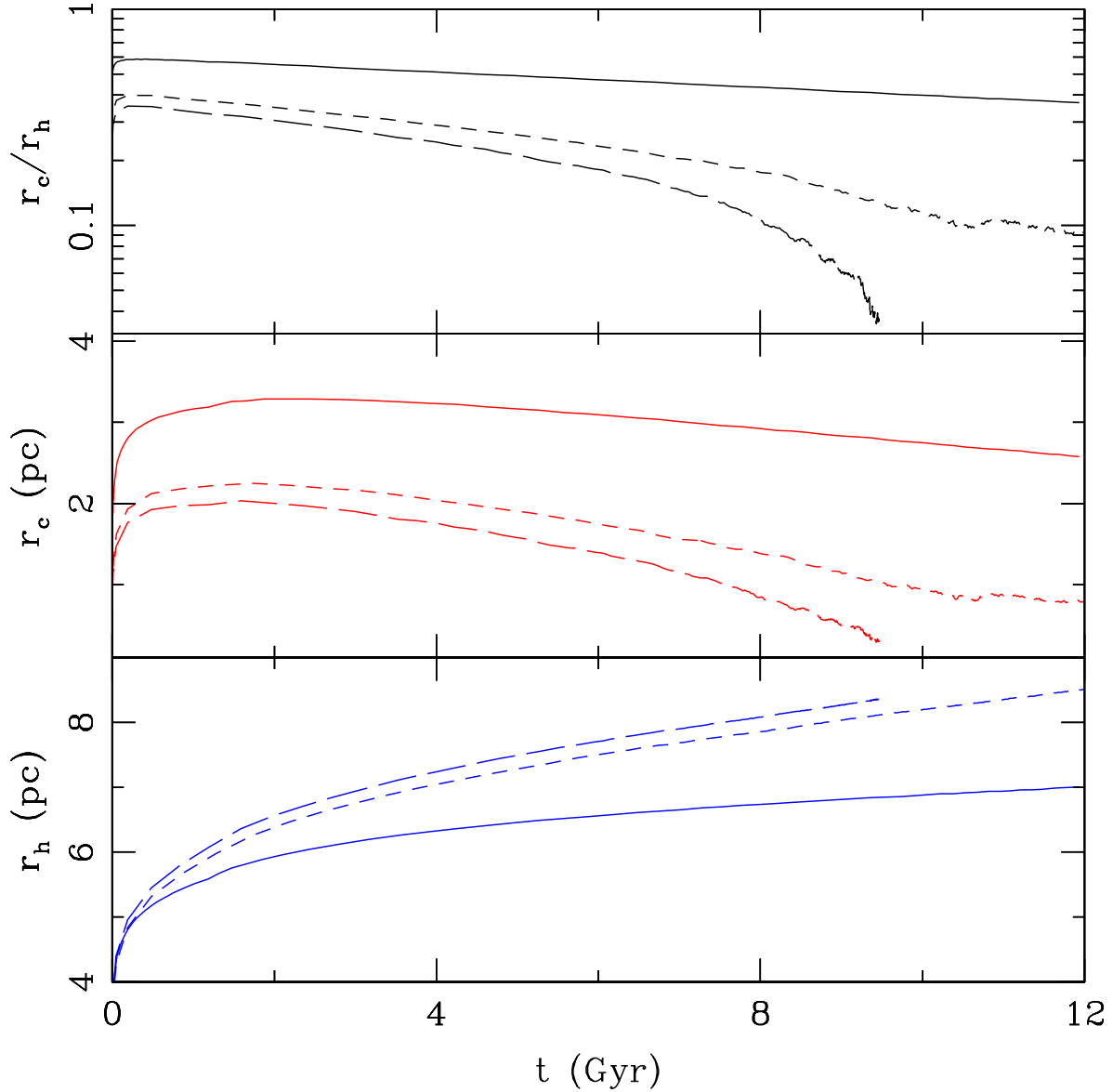


Fig. 14.— Evolution of  $r_c/r_h$  (top),  $r_c$  (middle) and  $r_h$  (bottom) for three qualitatively different clusters. Results from runs `c1f3n4`, `c3f2n1`, and `c8f1n1` are shown in all three panels with solid, short-dashed, and long-dashed lines, respectively. Runs `c1f3n4`, `c3f2n1`, and `c8f1n1` at their final stage of simulation are in the slow contraction, binary-burning, and deep-collapse phase, respectively.

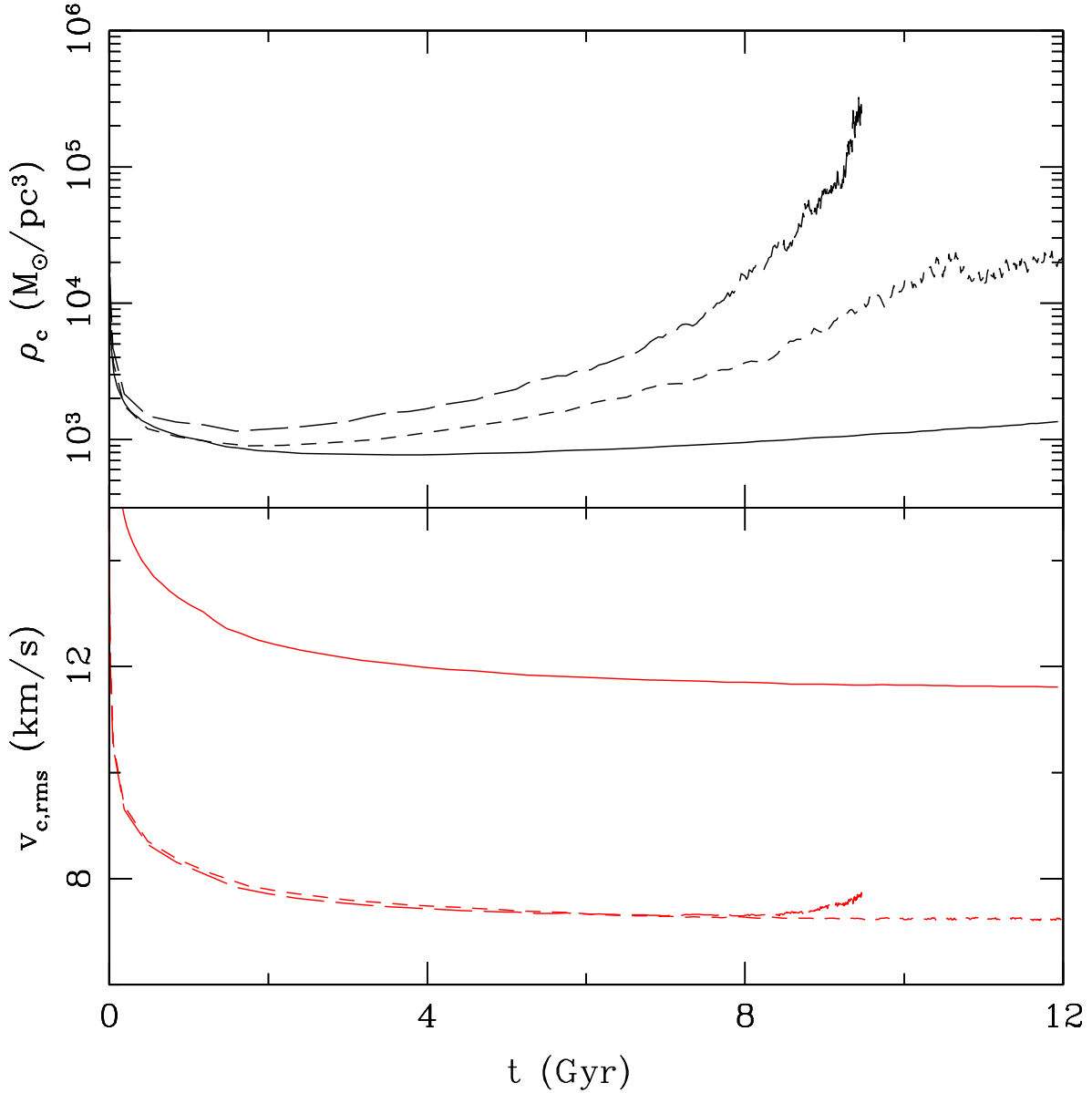


Fig. 15.— Evolution of the central stellar mass density ( $\rho_c$ , top) and the central r.m.s. velocity ( $v_{c,rms}$ , bottom) for three example runs **c1f3n4** (solid), **c3f2n1** (short-dashed), and **c8f1n1** (long-dashed).  $\rho_c$  and  $v_{c,rms}$  decrease sharply during the initial stellar evolution driven expansion of the clusters.  $\rho_c$  increases slowly during the slow-contraction phase. In the binary-burning phase  $\rho_c$  attains a quasi-steady value. A sharp increase in  $\rho_c$  is observed at the deep-collapse phase.  $v_{c,rms}$  remains more or less steady followed by the initial decrease. During deep-collapse  $v_{c,rms}$  increases sharply.

The central density for each simulated cluster first decreases sharply during the initial stellar evolution dominated phase due to the early expansion of the core. During the slow contraction phase the cluster stellar density increases steadily and reaches a quasi-steady value during the binary-burning phase (Figure 15). The central velocity dispersion ( $v_{c,rms}$ ) decreases sharply during the stellar evolution dominated phase. After that  $v_{c,rms}$  reaches a steady value of  $\sim 10$  km/s. The final value of  $v_{c,rms}$  depends on the evolutionary stage of the cluster as well as the total mass in the core. Note that the value of  $v_{c,rms}$  for runs **c3f2n1** and **c8f1n1** are similar, since the core masses are comparable, whereas a more massive cluster **c1f3n4** shows a higher  $v_{c,rms}$  as expected.  $v_{c,rms}$  for run **c8f1n1** starts to diverge from  $v_{c,rms}$  for run **c3f2n1** only when the former reaches the deep-collapse phase.

Figure 16 shows the surface density profiles for the total luminosity and number of stars for clusters **c1f3n4**, **c3f2n1**, and **c8f1n1** at the end of simulation. For the first two clusters the  $t_{cl} = 12$  Gyr. The third suffers a deep-collapse at  $\sim 9$  Gyr; the profile at the end of simulation is shown in that case. We find the best fit single-mass King profile parameters minimizing the  $\chi^2$  statistic from a grid of detailed King models, solving the Poisson equation where the mass density is calculated self-consistently (Miocchi 2006, the fitting program was kindly provided by Miocchi). Since for old GGCs and similarly for our simulated clusters the mass range of the stars at the final stage is narrow, a single-mass King profile is sufficiently accurate to predict the cluster parameters such as the King core radius and concentration (see Figure 16). Furthermore, we adopt a single-mass King fit since observers often follow this assumption (e.g., Dalessandro et al. 2008). The deep-collapsed cluster, **c8f1n1** clearly shows a very different projected density profile compared to the other two clusters and cannot be represented with a King density profile (Figure 16). The collapsed cluster do not have a well defined core as seen in the steady increase in the stellar number surface density. For cluster **c1f3n4**, which is in the slow contraction phase, a standard King density profile is an excellent representation of the simulated density profile. The density profile in the binary-burning cluster **c3f2n1** is close to a King profile, however, near the central region there is a hint of a power-law density profile expected from observed core-collapsed clusters. In this region, a power-law is a better representation than a King profile for this cluster indicating a self-similar collapse (Figure 16; e.g. Heggie & Hut 2003; Binney & Tremaine 2008).

We call the core radius and the concentrations calculated using the best fit King model as  $r_{c,obs}$  and  $c_{obs}$  respectively. Table 3 shows a full list of these values for all our simulated clusters. However, as shown in Figure 16 these values are not correct for the deep-collapsed clusters. Furthermore, for the binary burning clusters a King profile may not be a good fit. Nevertheless, most of our simulated clusters are in the slow contraction phase at  $t_{cl} = 12$  Gyr, where a King density profile is an excellent fit to the data. The luminosity profile is noisy due to the presence of a few high luminosity stars (Figure 16). If only stars with a stellar



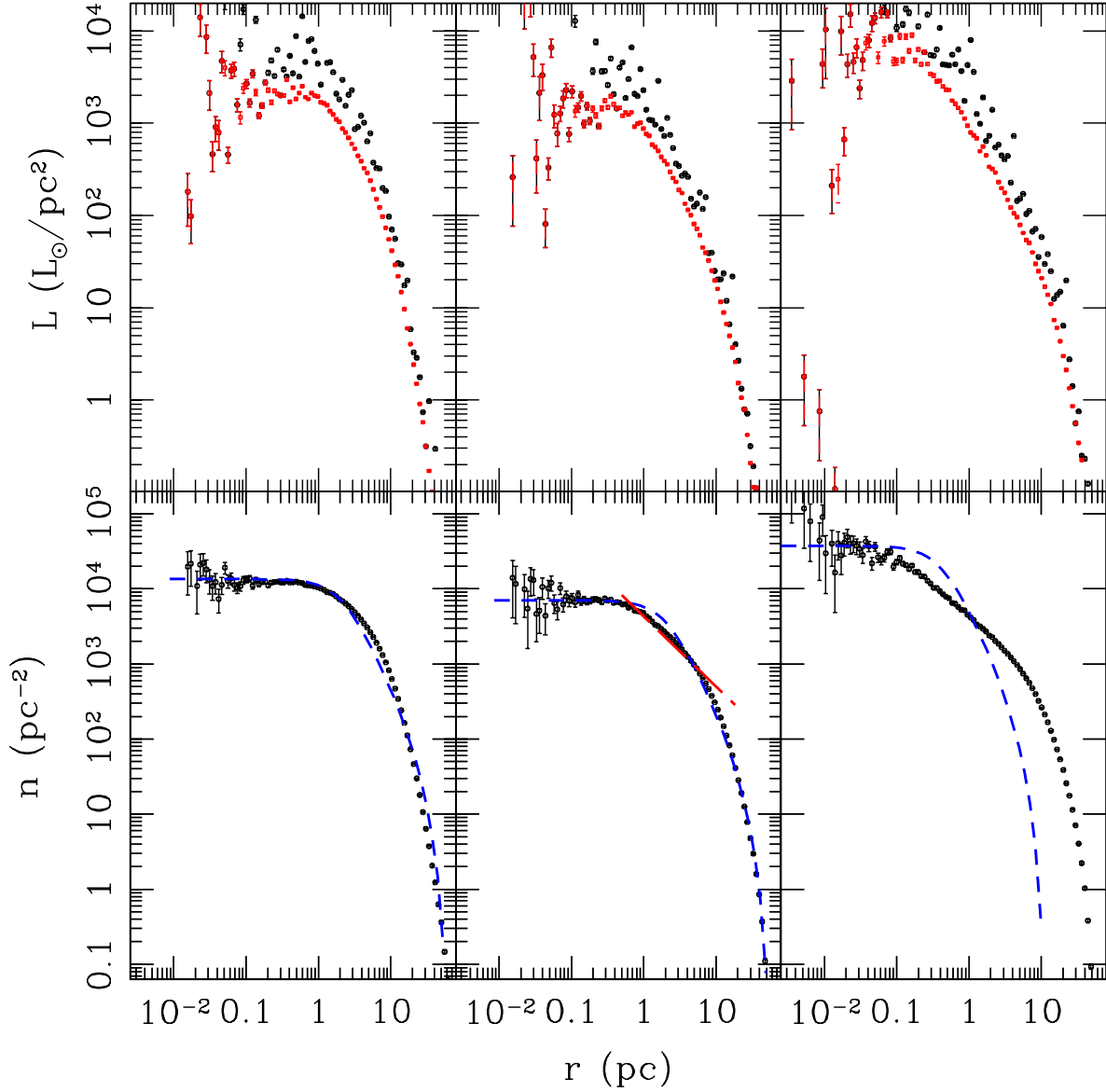


Fig. 16.— Radial profiles for the stellar luminosity density (top) and the stellar number density (bottom) at  $t_{cl} = 12$  Gyr for clusters **c1f3n4**, **c3f2n1**, and **c8f1n1**, from left to right, respectively. The error bars on each panel show the Poisson noise of the data. In the top panel the black circles show the luminosity density for all stars taken into account. The red squares show the luminosity density taking into account only stars with stellar luminosities  $L_* < 20 L_\odot$ . On each panel the dashed blue line shows the best fit King model to the data. Bottom left panel is a cluster in slow contraction phase and very well fitted by a King density profile. The bottom middle panel is a cluster in the binary burning phase. A King profile still works for most parts, however, a hint of a power-law profile is observed (red long dash). Bottom right panel is a deep-collapse cluster showing a power-law profile and a King profile is a very poor fit.

luminosity  $L_\star < 20 L_\odot$  are taken into account, the profile is less noisy.

The stellar properties such as the stellar luminosity and radius for each star in the simulated cluster are calculated in tandem with the dynamical evolution of the cluster using BSE (§2). From the stellar luminosity and the radius the black-body effective temperature can be calculated. Figure 17 shows an example of Hertzsprung-Russell diagram (HRD) obtained from the run `c1f3n4` at  $t_{cl} = 12$  Gyr. All binaries for this cluster are assumed to be unresolved. The effective temperature of a binary is approximated by a luminosity weighted average. Features of a realistic HRD including the MS of the stars, the binary sequence, giant branch, and single and binary white dwarf cooling sequences can be clearly seen. Moreover, exotic stars such as the BSSs are produced. Here, we define any MSS with a stellar mass  $M_\star > 1.1 M_{TO}$  for the cluster as a BSS and find that these stars populate the area of HRD expected from observations (Figure 18). Here  $M_{TO}$  is the MS turn-off mass for the cluster. We find that the numbers of BSSs in these clusters depend on the initial conditions as well as the evolutionary history. For example, clusters `c1f3n4`, `c3f2n1`, and `c8f1n1` host 52, 16, and zero BSSs, respectively, at the time when these snapshots were taken (12 Gyr for the first two and integration stopping time  $\approx 9$  Gyr for the third; Figure 18). A more systematic study on the correlations between the total number of BSSs and the cluster observable properties is underway.

## 6. Summary and Conclusion

We report the recent update in the development of the Hénon based MC code CMC, developed at Northwestern. We have added a fitting formulae based single and binary stellar evolution using BSE by Hurley et al. (2000, 2002) in addition to the already incorporated physical processes such as two-body relaxation and strong interaction including BS, BB and stellar collisions (Papers I–IV). Thus we are now able to model realistic dense massive clusters including all relevant physics with realistic stellar IMFs in our simulations. We test the code extensively and compare our results with previously published direct  $N$ -body results to validate CMC (§2.3,3).

In spite of the differences of the basic numerical methods we find that the agreement between CMC results and direct  $N$ -body results is excellent (in particular Figures 1-8). The close reproduction of the evolution of the core  $f_b$  and the overall  $f_b$  warrants special mention. The evolution of  $f_b$  is related to all physical processes relevant in the cluster. Two-body relaxation drives mass segregation. Binaries being more massive than typical single stars mass-segregate towards the center. In the core these binaries interact, and can get destroyed via BS/BB interactions. Throughout the evolution the cluster binaries evolve and can merge

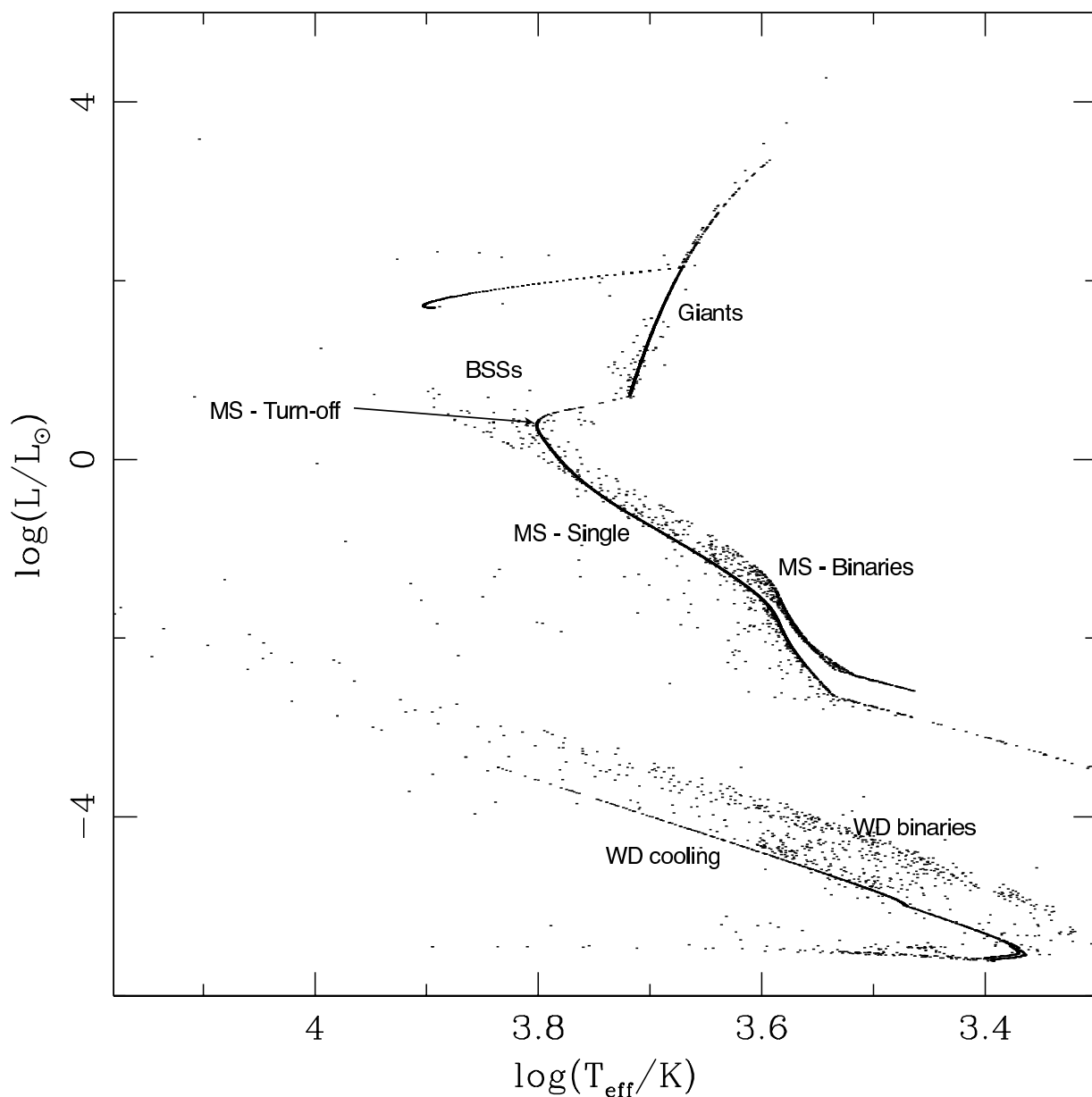


Fig. 17.— An example of a synthetic HRD for run `c1f3n4` from the set `fixed- $r_v$`  at  $t_{cl} = 12$  Gyr. Each dot is a bound object in the cluster (a single star or a binary). All binaries are assumed to be unresolved. The  $T_{\text{eff}}$  for a binary is the luminosity weighted temperature. The single and binary MSs of the cluster are clearly seen. The giant branch, WD cooling sequence, and BSSs are also observed. The stars in between the single MS and the WD binary sequence are binaries with MS and WD compact object components.

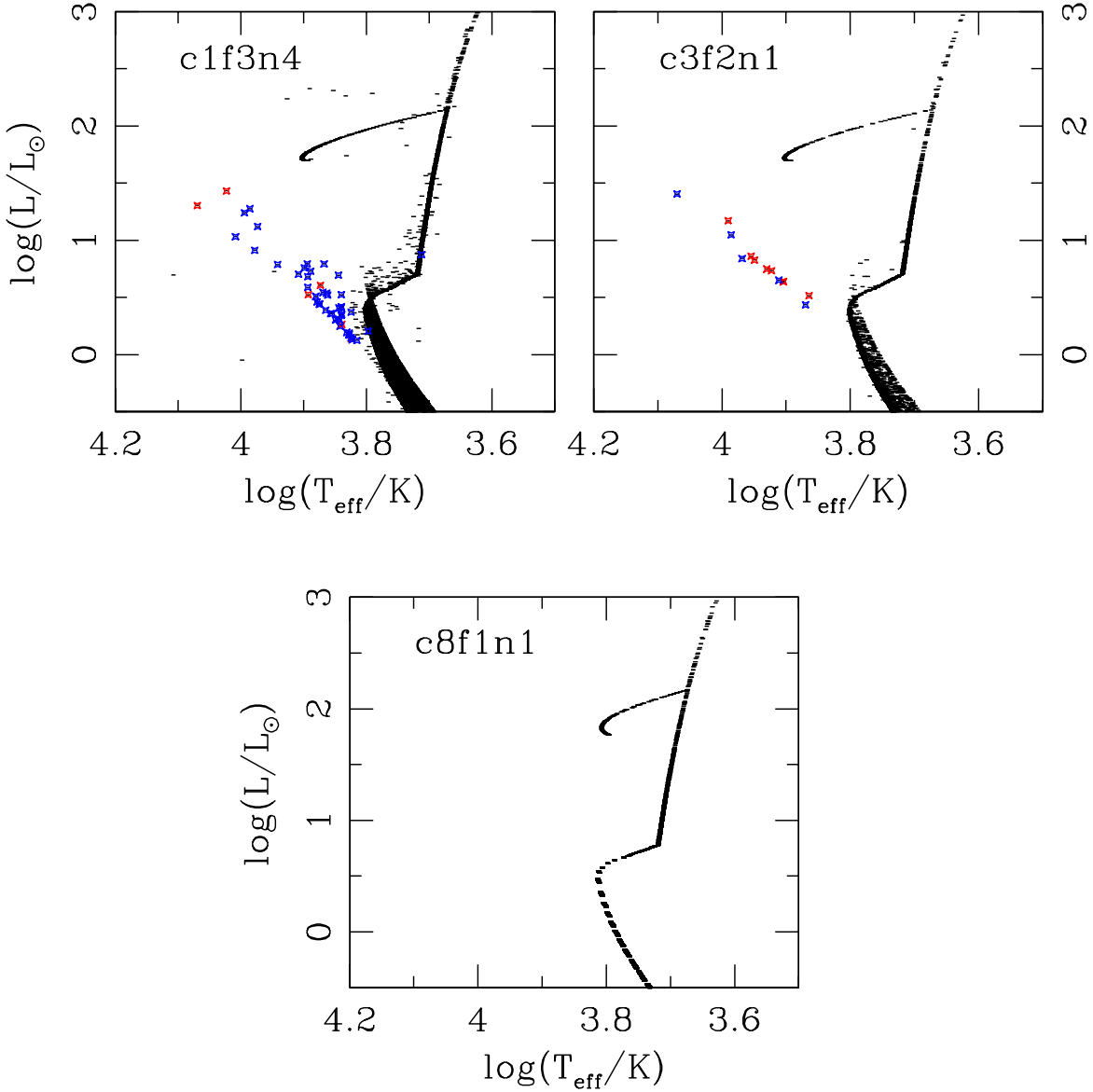


Fig. 18.— Synthetic HRD for the three sample simulated clusters `c1f3n4`, `c3f2n1`, and `c8f1n1`. For each of the HRDs the region near the tip of the MS is shown. Each dot is one bound object (single or binary) in the cluster. The BSSs for each cluster are shown as crosses; red and blue crosses denote single and binary BSSs. Here, BSSs are defined as the MSSs with mass  $m_{\star} > 1.1M_{TO}$  for the cluster at its age. Cluster `c1f3n4` has a higher number of BSSs among the three example clusters (7 singles, 45 binaries) because of this cluster’s higher  $N_i$  and initial  $f_b$  compared to cluster `c3f2n1` (9 singles, 7 binaries). Cluster `c8f1n1` has no BSSs at this age.

or disrupt simply through binary evolution. The galactic tidal field tidally strips low mass stars from the cluster tidal boundary. Thus obtaining the right evolution of  $f_b$  indicates all these physical processes are implemented correctly. In addition the close agreement between the fraction of double-degenerate binaries in the core (Figure 8) bolsters our belief that not only the dynamical processes are modeled correctly, but also stellar evolution and compact object formation are at least as accurate as the direct  $N$ -body code NBODY4.

Although the core properties are obtained accurately using CMC, a larger difference is found whenever a quantity involving the total number of bound stars in the cluster is compared. For example, the agreement in the evolution of the fractional number of bound stars, although is quite good (Figures 6, 7) given the drastically different methods of simulations, can differ by at most  $\approx 20\%$ . These differences are dominated by the tidal mass loss effects which is hard to model within MC methods and can only be addressed in a criterion based way (§2.3; also see e.g., Paper IV Giersz & Spurzem 2000). A more detailed study in characterizing the orbits in a cluster potential and tidal effects is underway, but is beyond the scope of this work.

Our results show that including stellar evolution and a realistic IMF dramatically change the evolution of a star cluster (§4) and to model a realistic star cluster, inclusion of this process is vital. The initial expansion of the cluster driven by stellar evolution mass loss significantly prolongs the slow contraction phase. Depending on the initial properties of the cluster, even without any primordial binaries the slow contraction phase may last more than a Hubble time for clusters typical for the GGCs (e.g., Figures 10, 12). On the contrary, exclusion of this important effect leads to a quick contraction of the cluster due to mass segregation even if only a moderately broad range of stellar IMF is used (Figure 10). We also show that even for simulations with a very narrow stellar mass range, for a relatively low  $f_b$  (Figure 9) the inclusion of stellar evolution can give  $r_c/r_h$  values  $\approx 10\%$  larger compared to when it is left out.

One of the biggest uncertainties of studying the evolution of dense, massive star clusters is in determining the initial conditions. The detailed evolution of a cluster depends on various initial properties including the initial effective radius, mass,  $f_b$ , concentration, and the galactic tidal field and estimating the initial conditions using the present day observed properties of a cluster is hard. Moreover, starting from different initial conditions it is possible to achieve very similar present day properties, e.g.,  $r_c$ , and  $r_c/r_h$  (Figures 12 and 13). In addition, the observed present day values can also be quite uncertain, especially the 3D orbit of a cluster in the galactic potential is hard to measure. Furthermore, although it may be possible to qualitatively understand individual effects of the various physical processes on the observable cluster properties, the collective effect is impossible to judge

without actual detailed simulations. Thus to understand a population of dense clusters it is required to study a large parameter space and study evolution of these cluster in a realistic way including all physics in tandem.

With the recent improvement to CMC it is now possible to truly scan the full parameter space realistically without any loss of generality due to its significantly lower computational cost compared to the direct  $N$ -body codes and the accuracy and ability to treat all relevant physical processes. We have started a detailed study to create a population of realistic globular clusters, representative of the observed GGCs with a large grid of simulations with realistic initial conditions motivated by observations of young massive clusters (e.g. Scheepmaker et al. 2007, 2009). Here we have presented some of these simulations to show that rather than creating specific clusters it is now beginning to be possible to create a whole population of GGCs using CMC in a star-by-star detail. We show that using observationally motivated initial conditions, without any need for fine tuning it is possible to create old dense clusters very similar to the observed GGCs (Figures 12 – 13).

Each star in CMC has realistic stellar properties such as luminosity, radius, and effective temperature in addition to the mass and position in the cluster (which is sufficient to follow its dynamics). Hence, in addition to the global evolution of the clusters it is possible to study individual stellar populations in a cluster. For example, we show synthetic HRDs for a few simulated clusters from our grid of simulations. All features, including, e.g., the single and binary MS, WD cooling sequence, the giant branch, and BSSs, of a realistic HRD can be seen in the synthetic HRD (Figures 17, 18). After this crucial improvement to CMC a large array of interesting problems are now accessible. For example, a detailed study of the observed GGC BSSs, their properties, and the correlations with various cluster properties is underway.

Table 3. List of simulations:  $W_0$  is the central concentration parameter for a King profile (King 1966), cluster mass  $M$  is in  $10^5 M_\odot$ , number of bound cluster objects  $N$  is given in  $10^5$ , central stellar mass density  $\rho_c$  is in  $10^3 M_\odot/\text{pc}^3$ ,  $r_c$  and  $r_h$  are in pc, and  $c$  is the concentration parameter defined as  $\log_{10}(r_c/r_t)$ . All final values are extracted from the final snapshot of the simulated clusters.  $r_{c,obs}$  and  $c_{obs}$  are estimated from a single-mass best fit King model to the  $2D$  number density at the final snapshot of the cluster.

Name	Initial									Final									
	$W_0$	$M$	$N$	$r_c$	$r_h$	$\rho_c$	$f_b$	$f_{b,c}$	$c$	$M$	$N$	$r_c$	$r_{c,obs}$	$r_h$	$\rho_c$	$f_b$	$f_{b,c}$	$c$	$c_{obs}$
c1f1n1	4	2.5	4	1.6	3.3	12.2	0.00	0.00	1.1	1.4	3	2.0	2.1	7.1	1.0	0.00	0.00	1.5	1.5
c1f1n2	4	3.8	6	1.6	3.3	16.2	0.00	0.00	1.5	2.1	5	2.3	2.2	7.0	1.1	0.00	0.00	1.5	1.5
c1f1n3	4	5.1	8	1.6	3.3	23.3	0.00	0.00	1.7	2.8	7	2.4	2.1	6.9	1.2	0.00	0.00	1.5	1.5
c1f1n4	4	6.4	10	1.6	3.3	29.0	0.00	0.00	1.6	3.5	9	2.5	2.0	6.8	1.4	0.00	0.00	1.5	1.6
c1f2n1	4	2.6	4	1.6	3.3	12.3	0.05	0.05	1.3	1.4	3	2.1	2.3	7.2	0.9	0.05	0.07	1.4	1.5
c1f2n2	4	3.9	6	1.6	3.3	17.3	0.05	0.05	1.6	2.1	5	2.3	2.2	7.1	1.1	0.05	0.07	1.5	1.5
c1f2n3	4	5.3	8	1.6	3.3	24.7	0.05	0.05	1.7	2.9	7	2.5	2.2	7.0	1.2	0.05	0.07	1.5	1.5
c1f2n4	4	6.6	10	1.6	3.3	30.2	0.05	0.05	1.7	3.6	9	2.5	2.0	6.9	1.4	0.05	0.06	1.5	1.6
c1f3n1	4	2.7	4	1.6	3.3	12.4	0.10	0.10	1.2	1.4	3	2.1	2.3	7.3	0.9	0.09	0.14	1.4	1.5
c1f3n2	4	4.0	6	1.6	3.3	17.7	0.10	0.10	1.3	2.2	5	2.3	2.2	7.2	1.1	0.09	0.14	1.5	1.5
c1f3n3	4	5.4	8	1.6	3.3	25.3	0.10	0.10	1.5	2.9	7	2.5	2.2	7.1	1.2	0.09	0.13	1.5	1.5
c1f3n4	4	6.8	10	1.6	3.3	30.9	0.10	0.10	1.7	3.7	9	2.6	2.1	7.0	1.4	0.09	0.12	1.5	1.5
c2f1n1	4.5	2.5	4	1.5	3.3	14.2	0.00	0.00	1.0	1.4	3	1.9	2.0	7.1	1.3	0.00	0.00	1.5	1.5
c2f1n2	4.5	3.8	6	1.5	3.3	18.8	0.00	0.00	1.5	2.1	5	2.1	2.0	7.0	1.4	0.00	0.00	1.5	1.5
c2f1n3	4.5	5.1	8	1.5	3.3	27.2	0.00	0.00	1.4	2.8	7	2.3	2.0	6.9	1.5	0.00	0.00	1.5	1.6
c2f1n4	4.5	6.4	10	1.5	3.3	33.3	0.00	0.00	1.4	3.5	9	2.3	2.0	6.9	1.7	0.00	0.00	1.5	1.6
c2f2n1	4.5	2.6	4	1.5	3.3	14.3	0.05	0.05	1.0	1.4	3	1.9	2.1	7.3	1.2	0.05	0.07	1.5	1.5
c2f2n2	4.5	3.9	6	1.5	3.3	20.1	0.05	0.05	1.7	2.1	5	2.2	2.1	7.2	1.3	0.05	0.07	1.5	1.5
c2f2n3	4.5	5.3	8	1.5	3.3	28.9	0.05	0.05	1.6	2.8	7	2.3	2.1	7.1	1.4	0.05	0.07	1.5	1.5
c2f2n4	4.5	6.6	10	1.5	3.3	34.7	0.05	0.05	1.7	3.6	9	2.4	2.0	7.0	1.7	0.05	0.07	1.5	1.6
c2f3n1	4.5	2.7	4	1.5	3.3	14.4	0.10	0.10	1.0	1.4	3	2.0	2.2	7.4	1.2	0.09	0.14	1.5	1.5
c2f3n2	4.5	4.0	6	1.5	3.3	20.5	0.10	0.10	1.8	2.2	5	2.2	2.1	7.3	1.3	0.09	0.14	1.5	1.5
c2f3n3	4.5	5.4	8	1.5	3.3	29.6	0.10	0.10	1.4	2.9	7	2.4	2.1	7.2	1.3	0.09	0.13	1.5	1.5
c2f3n4	4.5	6.8	10	1.5	3.3	35.4	0.10	0.10	1.4	3.7	9	2.4	2.0	7.1	1.7	0.09	0.13	1.5	1.6
c3f1n1	5	2.5	4	1.4	3.2	17.2	0.00	0.00	1.2	1.4	3	1.7	1.9	7.3	1.7	0.00	0.00	1.5	1.5
c3f1n2	5	3.8	6	1.4	3.3	22.4	0.00	0.00	1.4	2.1	5	2.0	2.0	7.1	1.7	0.00	0.00	1.5	1.6

Table 3—Continued

Name	Initial									Final									
	$W_0$	$M$	$N$	$r_c$	$r_h$	$\rho_c$	$f_b$	$f_{b,c}$	$c$	$M$	$N$	$r_c$	$r_{c,obs}$	$r_h$	$\rho_c$	$f_b$	$f_{b,c}$	$c$	$c_{obs}$
c3f1n3	5	5.1	8	1.4	3.3	32.5	0.00	0.00	1.7	2.8	7	2.1	2.0	7.0	1.9	0.00	0.00	1.6	1.6
c3f1n4	5	6.4	10	1.4	3.3	40.0	0.00	0.00	1.6	3.5	9	2.2	2.0	7.0	2.1	0.00	0.00	1.6	1.6
c3f2n1	5	2.6	4	1.4	3.2	17.3	0.05	0.05	1.3	1.4	3	1.7	2.1	7.4	1.7	0.05	0.08	1.5	1.5
c3f2n2	5	3.9	6	1.4	3.3	24.0	0.05	0.05	1.3	2.1	5	2.0	2.0	7.3	1.6	0.05	0.07	1.5	1.5
c3f2n3	5	5.3	8	1.4	3.3	34.6	0.05	0.05	1.5	2.8	7	2.2	2.0	7.2	1.8	0.05	0.07	1.5	1.6
c3f2n4	5	6.6	10	1.4	3.3	41.6	0.05	0.05	1.7	3.6	9	2.2	2.0	7.1	2.0	0.05	0.07	1.5	1.6
c3f3n1	5	2.7	4	1.4	3.2	17.4	0.10	0.10	1.5	1.4	3	1.8	2.1	7.6	1.5	0.09	0.15	1.5	1.5
c3f3n2	5	4.0	6	1.4	3.3	24.5	0.10	0.10	1.5	2.2	5	2.0	2.1	7.4	1.6	0.09	0.14	1.5	1.5
c3f3n3	5	5.4	8	1.4	3.3	35.4	0.10	0.10	1.4	2.9	7	2.2	2.1	7.3	1.8	0.09	0.13	1.5	1.6
c3f3n4	5	6.8	10	1.4	3.3	42.5	0.10	0.10	1.5	3.6	9	2.3	2.0	7.2	2.0	0.09	0.13	1.5	1.6
c4f1n1	5.5	2.5	4	1.3	3.2	21.6	0.00	0.00	1.2	1.4	3	1.5	1.8	7.4	2.5	0.00	0.00	1.6	1.6
c4f1n2	5.5	3.8	6	1.3	3.2	27.6	0.00	0.00	1.7	2.1	5	1.8	1.9	7.3	2.4	0.00	0.00	1.6	1.6
c4f1n3	5.5	5.1	8	1.3	3.3	40.2	0.00	0.00	1.4	2.8	7	1.8	2.0	7.2	2.9	0.00	0.00	1.6	1.6
c4f1n4	5.5	6.4	10	1.3	3.2	49.6	0.00	0.00	1.8	3.5	9	2.0	2.0	7.1	2.9	0.00	0.00	1.6	1.6
c4f2n1	5.5	2.6	4	1.3	3.2	21.7	0.05	0.05	1.6	1.4	3	1.6	1.9	7.6	2.1	0.05	0.08	1.5	1.6
c4f2n2	5.5	3.9	6	1.3	3.2	29.7	0.05	0.05	1.3	2.1	5	1.8	1.9	7.4	2.4	0.05	0.08	1.6	1.6
c4f2n3	5.5	5.3	8	1.3	3.3	43.0	0.05	0.05	1.6	2.8	7	1.9	2.0	7.3	2.6	0.05	0.08	1.6	1.6
c4f2n4	5.5	6.6	10	1.3	3.2	51.5	0.05	0.05	1.8	3.6	9	2.0	2.0	7.2	2.8	0.05	0.07	1.6	1.6
c4f3n1	5.5	2.7	4	1.3	3.2	21.7	0.10	0.10	1.3	1.4	3	1.6	1.9	7.7	2.0	0.09	0.15	1.5	1.6
c4f3n2	5.5	4.0	6	1.3	3.2	30.3	0.10	0.10	1.3	2.2	5	1.9	1.9	7.5	2.3	0.09	0.15	1.6	1.6
c4f3n3	5.5	5.4	8	1.3	3.3	44.0	0.10	0.10	1.3	2.9	7	2.0	2.0	7.4	2.5	0.09	0.14	1.6	1.6
c4f3n4	5.5	6.8	10	1.3	3.2	52.5	0.10	0.10	1.8	3.6	9	2.1	2.0	7.3	2.6	0.09	0.13	1.6	1.6
c5f1n1	6	2.5	4	1.2	3.2	28.5	0.00	0.00	1.4	1.4	3	1.2	1.4	7.6	4.9	0.00	0.00	1.7	1.7
c5f1n2	6	3.8	6	1.2	3.2	35.7	0.00	0.00	1.3	2.1	5	1.4	1.4	7.5	4.7	0.00	0.00	1.7	1.8
c5f1n3	6	5.1	8	1.2	3.2	52.8	0.00	0.00	1.4	2.8	7	1.6	1.9	7.4	4.5	0.00	0.00	1.7	1.6
c5f1n4	6	6.4	10	1.2	3.2	64.3	0.00	0.00	1.7	3.5	9	1.7	2.0	7.3	4.9	0.00	0.00	1.7	1.6



Table 3—Continued

Name	Initial									Final									
	$W_0$	$M$	$N$	$r_c$	$r_h$	$\rho_c$	$f_b$	$f_{b,c}$	$c$	$M$	$N$	$r_c$	$r_{c,obs}$	$r_h$	$\rho_c$	$f_b$	$f_{b,c}$	$c$	$c_{obs}$
c5f2n1	6	2.6	4	1.2	3.2	28.6	0.05	0.05	1.4	1.4	3	1.3	1.4	7.8	3.8	0.05	0.09	1.6	1.7
c5f2n2	6	3.9	6	1.2	3.2	38.5	0.05	0.05	1.3	2.1	5	1.5	1.9	7.7	4.1	0.05	0.08	1.6	1.6
c5f2n3	6	5.3	8	1.2	3.2	56.6	0.05	0.05	1.3	2.8	7	1.7	2.0	7.5	4.0	0.05	0.08	1.6	1.6
c5f2n4	6	6.6	10	1.2	3.2	66.5	0.05	0.05	1.7	3.6	9	1.8	2.0	7.4	4.3	0.05	0.07	1.6	1.6
c5f3n1	6	2.7	4	1.2	3.2	28.6	0.10	0.10	1.5	1.4	3	1.4	1.7	8.0	3.5	0.09	0.16	1.6	1.7
c5f3n2	6	4.0	6	1.2	3.2	39.3	0.10	0.10	1.3	2.2	5	1.6	1.9	7.8	3.8	0.09	0.16	1.6	1.6
c5f3n3	6	5.4	8	1.2	3.2	57.9	0.10	0.10	1.4	2.9	7	1.7	2.0	7.6	3.9	0.09	0.14	1.6	1.6
c5f3n4	6	6.8	10	1.2	3.2	67.9	0.10	0.10	1.8	3.8	9	2.3	1.9	6.9	1.9	0.09	0.13	1.5	1.6
c6f1n1	6.5	2.5	4	1.1	3.2	40.1	0.00	0.00	1.3	1.4	3	0.6	0.6	8.0	47.6	0.00	0.00	2.0	2.1
c6f1n2	6.5	3.8	6	1.1	3.2	49.3	0.00	0.00	1.4	2.1	5	1.1	1.2	7.7	9.7	0.00	0.00	1.8	1.8
c6f1n3	6.5	5.1	8	1.1	3.2	73.0	0.00	0.00	1.7	2.8	7	1.2	1.3	7.6	11.6	0.00	0.00	1.8	1.8
c6f1n4	6.5	6.4	10	1.1	3.2	88.8	0.00	0.00	1.6	3.5	9	1.3	1.3	7.5	9.4	0.00	0.00	1.8	1.8
c6f2n1	6.5	2.6	4	1.1	3.2	40.3	0.05	0.05	1.5	1.4	3	0.7	1.0	8.1	25.6	0.05	0.11	1.9	1.9
c6f2n2	6.5	3.9	6	1.1	3.2	53.4	0.05	0.05	1.4	2.1	5	1.1	1.3	7.9	9.6	0.05	0.09	1.7	1.8
c6f2n3	6.5	5.3	8	1.1	3.2	78.5	0.05	0.05	1.7	2.8	7	1.3	1.4	7.8	8.1	0.05	0.08	1.7	1.8
c6f2n4	6.5	6.6	10	1.1	3.2	91.7	0.05	0.05	1.6	3.6	9	1.4	1.4	7.7	8.7	0.05	0.08	1.7	1.8
c6f3n1	6.5	2.7	4	1.1	3.2	40.2	0.10	0.10	1.4	1.4	3	1.0	1.3	8.2	11.2	0.09	0.18	1.8	1.8
c6f3n2	6.5	4.0	6	1.1	3.2	54.4	0.10	0.10	1.4	2.2	5	1.2	1.5	8.0	8.3	0.09	0.16	1.7	1.8
c6f3n3	6.5	5.4	8	1.1	3.2	80.2	0.10	0.10	1.4	2.9	7	1.4	1.5	7.9	8.1	0.09	0.15	1.7	1.8
c6f3n4	6.5	6.8	10	1.1	3.2	93.6	0.10	0.10	1.6	3.6	9	1.4	1.4	7.8	9.4	0.09	0.15	1.7	1.8
c7f1n1	7	2.5	4	0.9	3.2	61.0	0.00	0.00	1.5	1.4	3	0.3	1.3	8.2	241.9	0.00	0.00	2.3	1.8
c7f1n2	7	3.8	6	0.9	3.3	73.4	0.00	0.00	1.5	2.1	5	0.3	1.0	8.2	314.0	0.00	0.00	2.3	1.9
c7f1n3	7	5.1	8	0.9	3.3	110.3	0.00	0.00	1.5	2.8	7	0.7	0.8	8.0	56.3	0.00	0.00	2.0	2.1
c7f1n4	7	6.4	10	0.9	3.3	134.5	0.00	0.00	1.6	3.5	9	0.8	0.8	7.9	54.2	0.00	0.00	2.0	2.1
c7f2n1	7	2.6	4	0.9	3.2	61.1	0.05	0.05	1.5	1.4	3	0.8	0.8	8.5	19.3	0.05	0.11	1.8	2.0
c7f2n2	7	3.9	6	0.9	3.3	79.7	0.05	0.05	1.9	2.1	5	0.7	0.9	8.3	43.3	0.05	0.11	1.9	2.0

We thank Jarrod Hurley for help with the BSE code and Paolo Miocchi for providing us with his fitting codes for single-mass King models. This work was supported by NASA Grants NNX08AG66G and NNG06GI62G at Northwestern University. JMF acknowledges support from Chandra/Einstein Postdoctoral Fellowship Award PF7- 80047. This research was partly done at KITP while the authors participated in the Spring 2009 program on Formation and Evolution of Globular Clusters, and was supported in part by NSF Grant PHY05-51164.

## REFERENCES

- Aarseth, S. J. 2003, *Gravitational N-Body Simulations*, ed. S. J. Aarseth
- Ashman, K. M. & Zepf, S. E. 2001, *AJ*, 122, 1888
- Baumgardt, H. & Makino, J. 2003, *MNRAS*, 340, 227
- Binney, J. & Tremaine, S. 2008, *Galactic Dynamics: Second Edition*, ed. J. Binney & S. Tremaine (Princeton University Press)
- Casertano, S. & Hut, P. 1985, *ApJ*, 298, 80
- Chatterjee, S., Fregeau, J. M., & Rasio, F. A. 2008, in *IAU Symposium*, Vol. 246, IAU Symposium, 151–155
- Dalessandro, E., Lanzoni, B., Ferraro, F. R., Vespero, F., Bellazzini, M., & Rood, R. T. 2008, *ApJ*, 681, 311
- Davis, D. S., Richer, H. B., Anderson, J., Brewer, J., Hurley, J., Kalirai, J. S., Rich, R. M., & Stetson, P. B. 2008, *AJ*, 135, 2155
- Demleitner, M., Accomazzi, A., Eichhorn, G., Grant, C. S., Kurtz, M. J., & Murray, S. S. 2001, in *Astronomical Society of the Pacific Conference Series*, Vol. 238, *Astronomical Data Analysis Software and Systems X*, ed. F. R. Harnden, Jr., F. A. Primini, & H. E. Payne, 321
- Eggleton, P. P., Tout, C. A., & Fitchett, M. J. 1989, *ApJ*, 347, 998
- Fregeau, J. M. 2008, *ApJ*, 673, L25
- Fregeau, J. M., Gürkan, M. A., Joshi, K. J., & Rasio, F. A. 2003, *ApJ*, 593, 772
- Fregeau, J. M., Ivanova, N., & Rasio, F. A. 2009, *ArXiv e-prints*, arXiv:0907.4196

Table 3—Continued

Name	Initial									Final									
	$W_0$	$M$	$N$	$r_c$	$r_h$	$\rho_c$	$f_b$	$f_{b,c}$	$c$	$M$	$N$	$r_c$	$r_{c,obs}$	$r_h$	$\rho_c$	$f_b$	$f_{b,c}$	$c$	$c_{obs}$
c7f2n3	7	5.3	8	0.9	3.3	118.9	0.05	0.05	1.5	2.8	7	0.9	1.1	8.2	29.5	0.05	0.10	1.9	1.9
c7f2n4	7	6.6	10	0.9	3.3	138.3	0.05	0.05	1.6	3.6	9	0.8	0.8	8.0	48.4	0.04	0.09	2.0	2.1
c7f3n1	7	2.7	4	0.9	3.2	60.8	0.10	0.10	1.7	1.4	3	0.9	1.1	8.6	17.4	0.09	0.19	1.8	1.8
c7f3n2	7	4.0	6	0.9	3.3	81.2	0.10	0.10	1.6	2.2	5	0.8	1.0	8.5	30.1	0.09	0.19	1.9	2.0
c7f3n3	7	5.4	8	0.9	3.3	121.3	0.10	0.10	1.5	2.9	7	1.1	1.2	8.2	15.9	0.09	0.17	1.8	1.8
c7f3n4	7	6.8	10	0.9	3.3	141.0	0.10	0.10	1.9	3.6	9	1.0	1.2	8.1	25.5	0.09	0.16	1.9	1.8
c8f1n1	7.5	2.5	4	0.7	3.3	103.6	0.00	0.00	1.6	1.4	3	0.3	0.4	8.4	267.0	0.00	0.00	2.3	2.3
c8f1n2	7.5	3.8	6	0.7	3.4	119.9	0.00	0.00	1.6	2.1	5	0.4	1.2	8.2	256.0	0.00	0.00	2.2	1.8
c8f1n3	7.5	5.1	8	0.7	3.4	181.1	0.00	0.00	1.6	2.8	7	0.4	1.0	8.2	275.1	0.00	0.00	2.2	1.9
c8f1n4	7.5	6.4	10	0.7	3.4	220.4	0.00	0.00	2.1	3.5	9	0.5	0.7	8.1	179.4	0.00	0.00	2.2	2.1
c8f2n1	7.5	2.6	4	0.7	3.3	103.6	0.05	0.05	1.6	1.4	3	0.7	0.9	8.9	27.0	0.05	0.11	1.9	2.0
c8f2n2	7.5	3.9	6	0.7	3.4	130.7	0.05	0.05	1.6	2.1	5	0.7	1.4	8.5	51.9	0.05	0.11	2.0	1.8
c8f2n3	7.5	5.3	8	0.7	3.4	195.8	0.05	0.05	1.6	2.8	7	0.8	1.2	8.3	44.3	0.05	0.10	1.9	1.8
c8f2n4	7.5	6.6	10	0.7	3.4	225.8	0.05	0.05	1.7	3.6	9	0.8	1.1	8.2	59.5	0.05	0.10	2.0	1.9
c8f3n1	7.5	2.7	4	0.7	3.3	103.0	0.10	0.10	1.6	1.4	3	0.9	1.3	8.9	18.4	0.09	0.20	1.8	1.8
c8f3n2	7.5	4.0	6	0.7	3.3	133.1	0.10	0.10	2.1	2.2	5	0.8	1.4	8.6	33.2	0.09	0.19	1.9	1.8
c8f3n3	7.5	5.4	8	0.7	3.4	199.3	0.10	0.10	1.6	2.9	7	0.9	1.3	8.4	40.9	0.09	0.18	1.9	1.8
c8f3n4	7.5	6.8	10	0.7	3.4	230.1	0.10	0.10	1.7	3.7	9	0.9	1.1	8.2	42.5	0.09	0.17	1.9	1.9

- Fregeau, J. M. & Rasio, F. A. 2007, *ApJ*, 658, 1047
- Freitag, M., Gürkan, M. A., & Rasio, F. A. 2006a, *MNRAS*, 368, 141
- Freitag, M., Rasio, F. A., & Baumgardt, H. 2006b, *MNRAS*, 368, 121
- Giersz, M. 1998, *MNRAS*, 298, 1239
- Giersz, M., Heggie, D. C., & Hurley, J. R. 2008, *MNRAS*, 388, 429
- Giersz, M. & Spurzem, R. 2000, *MNRAS*, 317, 581
- Harris, H. C., Harris, G. L. H., Hesser, J. E., & MacGillivray, H. T. 1984, *ApJ*, 287, 185
- Harris, W. E. 1996, *AJ*, 112, 1487
- Heggie, D. & Hut, P. 2003, *The Gravitational Million-Body Problem: A Multidisciplinary Approach to Star Cluster Dynamics* (Cambridge University Press, 2003)
- Heggie, D. C. & Giersz, M. 2008, *MNRAS*, 389, 1858
- Heggie, D. C., Trenti, M., & Hut, P. 2006, *MNRAS*, 368, 677
- Hénon, M. 1971a, *Ap&SS*, 13, 284
- Hénon, M. H. 1971b, *Ap&SS*, 14, 151
- Hesser, J. E., Harris, H. C., van den Bergh, S., & Harris, G. L. H. 1984, *ApJ*, 276, 491
- Hodge, P. W. 1962, *PASP*, 74, 248
- Hurley, J. R. 2007, *MNRAS*, 379, 93
- Hurley, J. R., Aarseth, S. J., & Shara, M. M. 2007, *ApJ*, 665, 707
- Hurley, J. R., Pols, O. R., & Tout, C. A. 2000, *MNRAS*, 315, 543
- Hurley, J. R., Tout, C. A., Aarseth, S. J., & Pols, O. R. 2001, *MNRAS*, 323, 630
- Hurley, J. R., Tout, C. A., & Pols, O. R. 2002, *MNRAS*, 329, 897
- Hwang, N. & Lee, M. G. 2008, *AJ*, 135, 1567
- Ivanova, N., Belczynski, K., Fregeau, J. M., & Rasio, F. A. 2005, *MNRAS*, 358, 572
- Ivanova, N., Heinke, C. O., Rasio, F. A., Belczynski, K., & Fregeau, J. M. 2008, *MNRAS*, 386, 553

- Ivanova, N., Heinke, C. O., Rasio, F. A., Taam, R. E., Belczynski, K., & Fregeau, J. 2006, *MNRAS*, 372, 1043
- Joshi, K. J., Nave, C. P., & Rasio, F. A. 2001, *ApJ*, 550, 691
- Joshi, K. J., Rasio, F. A., & Portegies Zwart, S. 2000, *ApJ*, 540, 969
- King, I. R. 1966, *AJ*, 71, 64
- Kroupa, P. 2001, *MNRAS*, 322, 231
- Kroupa, P., Gilmore, G., & Tout, C. A. 1991, *MNRAS*, 251, 293
- Lombardi, Jr., J. C., Rasio, F. A., & Shapiro, S. L. 1995, *ApJ*, 445, L117
- . 1996, *ApJ*, 468, 797
- Lombardi, Jr., J. C., Warren, J. S., Rasio, F. A., Sills, A., & Warren, A. R. 2002, *ApJ*, 568, 939
- Mackey, A. D., Wilkinson, M. I., Davies, M. B., & Gilmore, G. F. 2008, *MNRAS*, 374
- Mateo, M. 1987, *ApJ*, 323, L41
- Merritt, D., Piatek, S., Portegies Zwart, S., & Hemsendorf, M. 2004, *ApJ*, 608, L25
- Miller, G. E. & Scalo, J. M. 1979, *ApJS*, 41, 513
- Miocchi, P. 2006, *MNRAS*, 366, 227
- Salpeter, E. E. 1955, *ApJ*, 121, 161
- Scheepmaker, R. A., Gieles, M., Haas, M. R., Bastian, N., & Larsen, S. S. The Radii of Thousands of Star Clusters in M51 with HST/ACS, ed. T. Richtler & S. Larsen, 103
- Scheepmaker, R. A., Haas, M. R., Gieles, M., Bastian, N., Larsen, S. S., & Lamers, H. J. G. L. M. 2007, *A&A*, 469, 925
- Sills, A., Faber, J. A., Lombardi, Jr., J. C., Rasio, F. A., & Warren, A. R. 2001, *ApJ*, 548, 323
- Sills, A., Lombardi, Jr., J. C., Baily, C. D., Demarque, P., Rasio, F. A., & Shapiro, S. L. 1997, *ApJ*, 487, 290
- Spitzer, L. 1987, *Dynamical evolution of globular clusters*, ed. L. Spitzer

Trenti, M. 2006, ArXiv e-prints, arXiv:astro-ph/0612040v1

Trenti, M., Ardi, E., Mineshige, S., & Hut, P. 2007, MNRAS, 374, 857

van den Bergh, S., Morbey, C., & Pazder, J. 1991, ApJ, 375, 594

Vesperini, E. & Chernoff, D. F. 1994, ApJ, 431, 231